Remote Sensing of Environment 141 (2014) 243–261

Contents lists available at ScienceDirect

Remote Sensing of Environment

journal homepage: www.elsevier.com/locate/rse

A Surface Temperature Initiated Closure (STIC) for surface energy balance fluxes

Kaniska Mallick [a,*], Andrew J. Jarvis [b], Eva Boegh [c], Joshua B. Fisher [a], Darren T. Drewry [a], Kevin P. Tu [d], Simon J. Hook [a], Glynn Hulley [a], Jonas Ardö [e], Jason Beringer [f], Altaf Arain [g], Dev Niyogi [h]

[a] Jet Propulsion Laboratory, California Institute of Technology, 4800 Oak Grove Drive, Pasadena, CA 91109, United States
[b] Lancaster Environment Centre, Lancaster University, LA1 4YQ, United Kingdom
[c] Department of Environmental Social and Spatial Change, Roskilde University, Denmark
[d] Pioneer Hi-Bred International, Woodland, CA, United States
[e] Department of Physical Geography and Ecosystems Science, Lund University, Sweden
[f] School of Geography and Environmental Science, Monash University, Clayton, Victoria 3800, Australia
[g] School of Geography and Earth Sciences, McMaster University, Ontario, Canada
[h] Department of Agronomy and Earth Atmospheric Planetary Sciences, Purdue University, West Lafayette, IN, United States

ARTICLE INFO

Article history:
Received 19 November 2012
Received in revised form 11 September 2013
Accepted 25 October 2013

Keywords:
Surface energy balance
Penman–Monteith equation
Advection–aridity hypothesis
Boundary layer conductance
Surface conductance
MODIS
Land surface temperature
FLUXNET
Evapotranspiration

ABSTRACT

The use of Penman–Monteith (PM) equation in thermal remote sensing based surface energy balance modeling is not prevalent due to the unavailability of any direct method to integrate thermal data into the PM equation and due to the lack of physical models expressing the surface (or stomatal) and boundary layer conductances (g_S and g_B) as a function of surface temperature. Here we demonstrate a new method that physically integrates the radiometric surface temperature (T_S) into the PM equation for estimating the terrestrial surface energy balance fluxes (sensible heat, H and latent heat, λE). The method combines satellite T_S data with standard energy balance closure models in order to derive a hybrid closure that does not require the specification of surface to atmosphere conductance terms. We call this the Surface Temperature Initiated Closure (STIC), which is formed by the simultaneous solution of four state equations. Taking advantage of the psychrometric relationship between temperature and vapor pressure, the present method also estimates the near surface moisture availability (M) from T_S, air temperature (T_A) and relative humidity (R_H), thereby being capable of decomposing λE into evaporation (λE_E) and transpiration (λE_T). STIC is driven with T_S, T_A, R_H, net radiation (R_N), and ground heat flux (G). T_S measurements from both MODIS Terra (MOD11A2) and Aqua (MYD11A2) were used in conjunction with FLUXNET R_N, G, T_A, R_H, λE and H measurements corresponding to the MODIS equatorial crossing time. The performance of STIC has been evaluated in comparison to the eddy covariance measurements of λE and H at 30 sites that cover a broad range of biomes and climates. We found a RMSE of 37.79 (11%) (with MODIS Terra T_S) and 44.27 W m^{-2} (15%) (with MODIS Aqua T_S) in λE estimates, while the RMSE was 37.74 (9%) (with Terra) and 44.72 W m^{-2} (8%) (with Aqua) in H. STIC could efficiently capture the λE dynamics during the dry down period in the semi-arid landscapes where λE is strongly governed by the subsurface soil moisture and where the majority of other λE models generally show poor results. Sensitivity analysis revealed a high sensitivity of both the fluxes to the uncertainties in T_S. A realistic response and modest relationship was also found when partitioned λE components (λE_E and λE_T) were compared to the observed soil moisture and rainfall. This is the first study to report the physical integration of T_S into the PM equation and finding analytical solution of the physical (g_B) and physiological conductances (g_S). The performance of STIC over diverse biomes and climates points to its potential to benefit future NASA and NOAA missions having thermal sensors, such as HyspIRI, GeoSTAR and GOES-R for mapping multi-scale λE and drought.

© 2013 Elsevier Inc. All rights reserved.

1. Introduction

Quantitative understanding of the behavior of the latent and sensible heat fluxes is central to a broad range of applications including water resource management (Anderson, Norman, Mecikalski, Otkin & Kustas, 2007; French, Schmugge, Kustas, Brubaker & Prueger, 2003; Norman, Kustas & Humes, 1995), weather forecasting and climate change prediction (Entekhabi, Asrar, Betts, Beven, Bras, Duffy, et al., 1999). The Penman–Monteith (PM) equation (Monteith, 1965) has become the pre-eminent method for specifying the surface to air latent heat flux, λE, (or evapotranspiration, E), in a broad range of applications (Choudhury, 1997; Droogers & Allen, 2002; Eslamian, Gohari, Zareian & Firoozfar, 2012, Moran, Rahman, Washburne, Goodrich, Weltz & Kustas, 1996). The central concept in the derivation of this combination

* Corresponding author. Tel.: +1 818 331 8672, +1 818 354 1129.
E-mail address: kaniska.mallick@gmail.com (K. Mallick).

0034-4257/$ – see front matter © 2013 Elsevier Inc. All rights reserved.
http://dx.doi.org/10.1016/j.rse.2013.10.022

equation is the elimination of the need to specify surface temperature (T_S) when estimating λE. This was originally motivated by the fact that observations of T_S were invariably lacking for the scales at which λE is needed to be specified (Monteith, 1965).

However, in solving this problem the PM approach creates further problems, particularly in relation to the specification of the boundary layer (or aerodynamic) and surface (or stomatal) conductance terms (g_B and g_S) which are generally not measureable at scales in which the PM equation is applied. The principal solution to this has been the adoption of somewhat speculative models for these conductances, degrading the predictive quality of the PM framework. The speculative nature of the models for g_B stems from several sources (Cleugh, Leuning, Mu & Running, 2007; Mu, Heinsch, Zhao & Running, 2007; Su, 2002) and although credible models for mass, momentum and energy transfer exist (Liu, Lu, Mao & Jia, 2007) these require parameterization in order to make them applicable to the intended scale of use (Raupach & Finnigan, 1995). Furthermore, these parameterizations are not stationary due to the dynamics of the near surface and its boundary layer. For g_S the situation is more problematic in that, in addition to the scale dependence and spatiotemporal heterogeneity, there remains no universally agreed quantitative model that describes the biological controls on water and carbon fluxes (Landsberg, Kaufman, Binkeley, Isebrands & Jarvis, 1991) despite mechanistic (Dewar, 1995; Katul, Manzoni, Palmroth & Oren, 2010; Leuning, 1995) and empirical (Ball, Woodrow & Berry, 1987; Jarvis, 1976) models being widely used.

The nature of the elimination of T_S from the PM equation arises from the fact that the physical feedbacks regulating λE are heavily temperature dependent, making T_S a primary state variable of surface energy balance closures (Kustas & Anderson, 2009). As a result, in situations where observations of T_S are available, such as from remote sensing platforms, this provides a rich source of information that can be exploited to characterize the components of surface energy balance. Recognizing this, and motivated by the advent of thermal remote sensing, an alternative modeling strategy for λE has been to use T_S to solve for the sensible heat flux (H) and then estimate λE as a residual of the surface energy balance (Anderson et al., 1997, 2007; Bastiaansssen, Menenti, Feddes & Holtslag, 1998; Kustas & Norman, 1999; Norman et al., 1995; Su, 2002). So, although Hall et al. (1992) expressed serious doubts over using remotely sensed T_S measurements in aerodynamic transfer equations because of the large differences that can exist between the radiometric, T_{SR}, and aerodynamic, T_{SA}, surface temperatures (Troufleau et al., 1997), using a two—source soil-canopy framework (Anderson et al., 1997, 2007; Norman et al., 1995) and inclusion of an 'extra conductance' concept in the single—source framework (Boegh, Soegaard & Thomsen, 2002; Su, 2002) appeared to accommodate the effects of differences between T_{SR} and T_{SA}.

However, although useful, the above approaches still rely on the specification of g_B as an exogenous input when clearly it is an internal variable whose state is closely related to that of T_S. Therefore, an alternative approach may be to revisit the PM framework to see if T_S can be used to eliminate the need to specify g_B and g_S altogether. This paper focuses on attempting to solve the PM closure problem in such a way that treats g_B and g_S as internal unobserved components and instead exploits remotely sensed observations of T_S. For this we combine the PM framework with the advection–aridity hypothesis of Brutsaert & Stricker (1979), which is a modification of Bouchet's complementary hypothesis (Bouchet, 1963). This approach is based on the PMBL (Penman–Monteith–Bouchet–Lhomme) method proposed by Mallick, Jarvis, Fisher, Tu, Boegh & Niyogi (2013) where relative humidity (R_H) and atmospheric vapor pressure deficit (D_A) information were used to describe the 'wetness' of the land surface. The T_S variant of PMBL considered here uses T_S as an additional data source to obtain the system closure through retrieving the 'near surface' moisture availability (M) and 'effective' vapor pressure at the evaporating front (e_S) (vapor pressure at the level of T_S measurements). We refer the scheme as the Surface Temperature Initiated Closure (STIC). The study objectives of the paper are:

(1) To derive a surface energy balance closure expression for λE building on the PM equation framework but re-incorporating T_S in order to eliminate the exogenous expressions for g_B and g_S.
(2) To evaluate the estimates of λE and H produced by this closure using tower flux data from a broad range of biome and climate types, including a sensitivity analysis to input errors.
(3) To evaluate some of the components generated by STIC, in particular evaporation, transpiration, and land surface wetness in comparison with observed hydrological variables (e.g., soil moisture and rainfall).

Section 2 sets out the derivation of STIC. Section 3 describes the data sources used in the study. Section 4 describes a sensitivity analysis of STIC, the evaluation of STIC outputs against the tower measurements and a putative evaluation of the ancillary STIC outputs. Study results are discussed in Section 5, while the strengths and limitations of the proposed approach are described in Section 6. A list of symbols used in the present study is given in Table 1.

Table 1
Table of symbols and their description used in the study.

Symbol	Description
λ	Latent heat of vaporization of water (j kg^{-1} K^{-1})
λE	Evaporation (evaporation + transpiration) as latent heat flux (W m^{-2})
H	Sensible heat flux (W m^{-2})
R_N	Net radiation (W m^{-2})
R_G	Shortwave radiation (W m^{-2})
G	Ground heat flux (W m^{-2})
Φ	Net available energy (W m^{-2})
E	Evapotranspiration (evaporation + transpiration) as depth of water (mm)
λE_E	Evaporation as flux (W m^{-2})
λE_T	Transpiration as flux (W m^{-2})
λE^*	Potential evaporation as flux (W m^{-2})
λE_T^*	Potential transpiration as flux (W m^{-2})
λE_W	Wet environment evaporation as flux (W m^{-2})
λE_P^*	Potential evaporation as flux (W m−2) according to Penman
λE_{PT}^*	Potential evaporation as flux (W m−2) according to Priestley–Taylor
E_E	Evaporation as depth of water (mm)
E_T	Transpiration as depth of water (mm)
E^*	Potential evaporation as depth of water (mm)
E_T^*	Potential transpiration as depth of water (mm)
E_P^*	Potential evaporation as depth of water (mm) according to Penman
E_{PT}^*	Potential evaporation as depth of water (mm) according to Priestley–Taylor
E_W	Wet environment evaporation as depth of water (mm)
g_B	Boundary layer conductance (m s^{-1})
g_S	Stomatal/surface conductance (m s^{-1})
M	Surface moisture availability (0–1)
T_A	Air temperature (°C)
T_D	Dewpoint temperature (°C)
T_S	Radiometric surface temperature (°C)
T_{SD}	Surface dew-point temperature (°C)
T_{SA}	Aerodynamic surface temperature (°C)
T_{SR}	Radiometric surface temperature (°C)
R_H	Relative humidity (%)
e_A	Atmospheric vapor pressure (hPa) at the level of T_A measurement
D_A	Atmospheric vapor pressure deficit (hPa) at the level of T_A measurement
e_S	'effective' vapor pressure of evaporating front near the surface (hPa)
e_S^*	Saturation vapor pressure of surface (hPa) at T_S
s	Slope of saturation vapor pressure versus temperature curve (hPa K^{-1})
γ	Psychrometric constant (hPa K^{-1})
ρ	Density of air (kg m^{-3})
c_p	Specific heat of dry air (MJ kg^{-1} K^{-1})
Λ	Evaporative fraction
β	Bowen ratio
θ	Surface (0–5 cm) soil moisture (m^3 m^{-3})
θ_d	Deep layer (15–30 cm) soil moisture (m^3 m^{-3})
L	Leaf area index

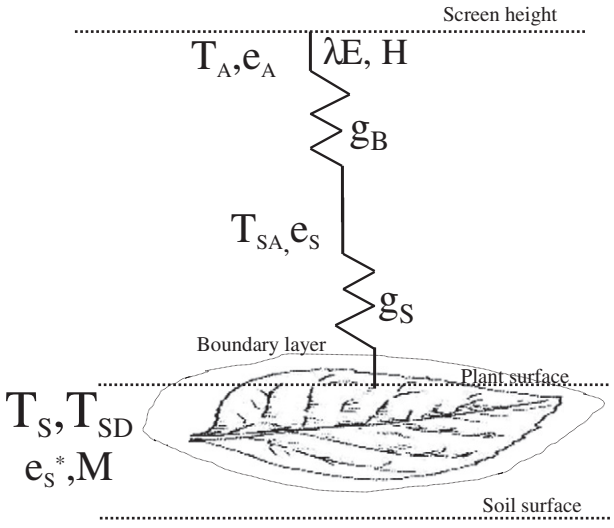

Fig. 1. Schematic representation of one-dimensional description of STIC. Here g_B and g_S are the aerodynamic and stomatal conductances, e_S^* is the saturation vapor pressure of the surface, T_{SA} is the aerodynamic surface temperature that is responsible for transferring the sensible heat (H), e_S is the near surface vapor pressure of the evaporating front, T_S is the radiometric surface temperature, T_{SD} is the surface dewpoint temperature, M is the surface moisture availability, T_A and e_A are temperature and vapor pressure of reference height, and λE is the latent heat flux, respectively.

2. Derivation of STIC

The conceptual framework for STIC is given in Fig. 1. The aim here is to define a surface energy balance equation set that treats g_B and g_S as internal states and T_S as external to the solution. This set will consist of four equations and four unknowns which will be solved analytically. The four unknowns are; g_B; g_S; the vertical difference between the source/sink height temperature (T_{SA}) (also called the aerodynamic temperature) and air temperature (T_A), ΔT; and the evaporative fraction, Λ.

The PM equation states (Monteith, 1965),

$$\lambda E = \frac{s\Phi + \rho c_P g_B D_A}{s + \gamma\left(1 + \frac{g_B}{g_S}\right)} \tag{1}$$

where ρ is the density of dry air (kg m^{-3}), c_P is the specific heat of dry air (MJ kg^{-1} K^{-1}), γ is the psychrometric constant (hPa K^{-1}), s is the slope of the saturation vapor pressure versus air temperature (hPa K^{-1}), D_A is the saturation deficit of the air (hPa) at the reference level and Φ is the net available energy (W m^{-2}) (the difference between net radiation, R_N and ground heat flux, G). The two unknowns in Eq. (1) are g_B and g_S and derivations of the physical expressions for these two unknowns are given in Appendix A (see also Mallick et al., 2013). However, these expressions require specification of the near surface moisture availability, M and evaporative fraction, Λ.

M is a unitless quantity which signifies the relative dryness or wetness of the surface and hence controls the potential evaporation rate. Considering the general case of evaporation from any nonsaturated surface at a rate less than the potential, M is the ratio of the evaporation rate, E, to the potential evaporation rate, E^*. M is assumed to be homogeneous between the surface and the evaporation front and its contribution to the effective vapor pressure of the evaporating front near the surface (e_S) is given as follows (Lee & Pielke, 1992; Segal, Jia, Ye & Pielke, 1990).

$$e_S = e_A(1-M) + Me_S^* \tag{2}$$

where e_S^* is the saturation vapor pressure at the surface (hPa), normally expressed as a function of T_S, and e_A is the atmospheric vapor pressure (hPa) at the level at which T_A is measured. $M = 0$ indicates complete dryness whereas $M = 1$ reflects a saturated evaporating front ($e_S \rightarrow e_S^*$) (i.e., after a heavy rainfall event or irrigation). When the evaporating front is absolutely dry $e_S = e_A$. Since $e_A > 0$, the initial moisture gradient towards the evaporating front eventually results in $e_S = e_A$ (no dew is formed during the day). When $e_S = e_A$, no latent heat flux is transported from the surface to the atmosphere, as anticipated in the case of a dry surface.

Fisher, Tu & Baldocchi (2008) proposed an empirical expression for M in terms of D_A and R_H ($M = R_H^{D_A}$), assuming equilibrium between the surface moisture and atmospheric moisture. An atmosphere with low D_A and high R_H indicates a moist humid atmosphere, but the underlying surface may be intermediately dry to very dry. According to the Fisher et al. (2008) expression for M, such cases will portray a wet surface condition when actually it may be dry leading to λE being overestimated. Similarly an atmosphere with high D_A and low R_H will portray a dry surface condition when actually it is wet, leading to λE being underestimated. The surface and atmospheric moisture may only correspond when soil moisture is tightly coupled to the atmospheric moisture or radiation (Small & Kurc, 2003). As a result, although useful, the Fisher et al. (2008) expression generally results in the overestimation of λE for D_A ranging from 10 to 20 hPa and above (Mallick et al., 2013). Because T_S is far more sensitive to the land surface moisture conditions (Kustas & Anderson, 2009), here we use T_S in conjunction with T_A and R_H to attempt to retrieve M within a physical framework. T_S serves as a direct metric for the soil moisture status and vegetation conditions, which in turn influences the surface energy fluxes and their partitioning (Kustas & Anderson, 2009).

The retrieval of M and the expression for Λ is a key novelty of the STIC framework and hence these are described in detail in the main body of the paper. The equations for rest of the variables and their derivations are described in Appendix A.

2.1. Derivation of M

Like Fisher et al. (2008) we hypothesize that the moisture availability at the surface and at the evaporating front are similar and, therefore, M is derived from the surface–atmosphere information. According to Noilhan & Planton (1989), Ye & Pielke (1993) and Boegh et al. (2002), the transfer of λE from the surface can be written as follows.

$$\lambda E = \frac{\rho c_P}{\gamma} g_B(e_S - e_A) = ME_P = \frac{\rho c_P}{\gamma} M g_B(e_S^* - e_A) \tag{3}$$

From Eq. (3), a physical expression for M is given in terms of the vapor pressure gradients.

$$M = \frac{(e_S - e_A)}{(e_S^* - e_A)} \tag{4}$$

The main difficulty in applying Eq. (4) is that e_S is unknown and there is no straightforward way to relate e_S to T_S. Although the Clausius–Clapeyron relationship between vapor pressure and surface temperature is not linear, it is generally linearized for small temperature differences (Monteith, 1965). Fig. 2(a and b) shows the relationships between e_S, e_S^* and e_A and their corresponding temperatures. By analogy to the dew point temperature, T_D, if the surface air is brought to saturation without affecting e_S then $e_S = f\{T_{SD}\}$. Thus, $T_{SD} < T_S$ for unsaturated surface and $T_{SD} \rightarrow T_S$ as the surface tends to saturation. Therefore, e_S is the surface saturation vapor pressure at some notional surface dew point T_{SD}. Although T_{SD} cannot be directly measured, it can be derived from the slope of the relevant temperature–saturation vapor pressure curve. Therefore, from Eq. (4), Fig. 2, and following Monteith (1965), M can be written as follows,

$$M = \frac{(e_S - e_A)}{(e_S^* - e_A)} = \frac{s_1(T_{SD} - T_D)}{s_2(T_S - T_D)} \tag{5}$$

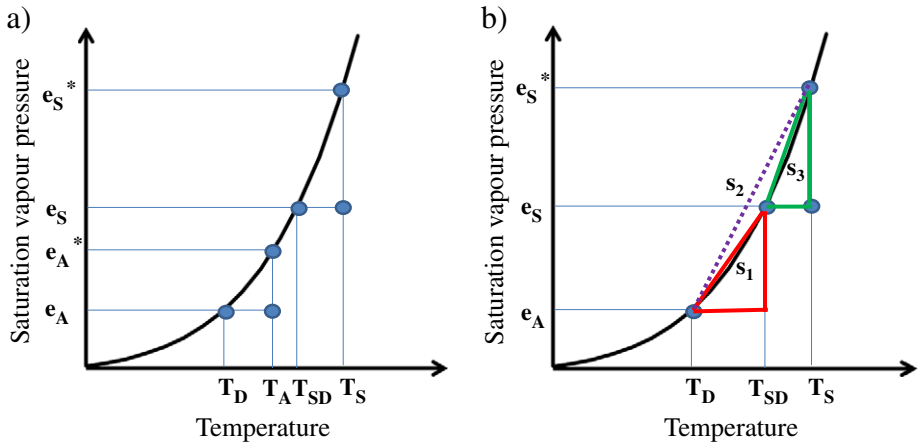

Fig. 2. (a) Conceptual diagram of the saturation vapor pressure curve and the relationship among T_{SD}, T_S, e_S and e_S^* in the context of surface at temperature T_S according to Venturini et al. (2008). The air and dewpoint temperature of the overlying air is characterized by T_A and T_D with the vapor pressure e_A and e_A^*. Here T_{SD} is the surface dew point temperature, T_S is the radiometric surface temperature, e_S is the near surface vapor pressure and e_S^* is the surface saturation vapor pressure. (b) Conceptual diagram of the linearized saturation vapor pressure curve to demonstrate the relationship between $(e_S - e_A)$ with $s_1(T_{SD} - T_D)$, $(e_S^* - e_S)$ with $s_3(T_S - T_{SD})$ and $(e_S^* - e_A)$ with $s_2(T_S - T_D)$. Here s_1, s_2, and s_3 are the slope of the saturation vapor pressure and temperature curve linearized according to Monteith (1965).

where s_1 and s_2 are the slopes of the saturation vapor pressure and temperature between $(T_{SD} - T_D)$ versus $(e_S - e_A)$ and $(T_S - T_D)$ versus $(e_S^* - e_A)$ relationship. For a dry surface $T_S \gg T_{SD}$, $e_S^* \gg e_S$, $(T_S - T_D) \gg (T_{SD} - T_D)$ and $M \to 0$. For any wet surface $e_S^* \cong e_S$, $T_S \cong T_{SD}$, $(T_S - T_D) \cong (T_{SD} - T_D)$ and $M \to 1$. According to Eq. (5), when condensation occurs, the surface temperature goes below the ambient air temperature and $e_S < e_A$, otherwise $e_S \geq e_A$ and $e_S \leq e_S^*$. Hence, T_{SD} falls somewhere between T_S and T_D (Fig. 2a) and can be computed by linearizing the saturation vapor pressure curve between the two levels (T_D, T_{SD}) and (T_{SD}, T_S) (Monteith, 1965).

Earlier, Venturini, Islam & Rodriguez (2008) assumed $s_1 = s_2$ and hence they cancel each other. Here, both the s_1 and s_2 are approximated from the corresponding Clausius–Clapeyron relationships. Since T_S and e_A are available, s_2 can be calculated directly. According to Fig. 2,

$$s_1 = \frac{(e_S - e_A)}{(T_{SD} - T_D)} \tag{6}$$

$$s_3 = \frac{(e_S^* - e_S)}{(T_S - T_{SD})} \tag{7}$$

Combining Eqs. (6) and (7) we can find an expression of T_{SD}.

$$T_{SD} = \frac{(e_S^* - e_A) - s_3 T_S + s_1 T_D}{(s_1 - s_3)} \tag{8}$$

Among the various exponential functions that relate the saturation vapor pressure and temperature, Buck's (Buck, 1981) equation was used for its simplicity. After estimating the saturation vapor pressure at different temperatures, the initial values of s_1 and s_3 are specified at T_D and T_S. Then using Eq. (8) an initial value of T_{SD} is obtained. The process is then iterated by updating s_3 with the first estimate of T_{SD} and computing a new T_{SD}. A large proportion of the saturation vapor pressure curve is assumed to be linearized in the first calculation and therefore s_1 is not updated. Repeating this process produces stable values of T_{SD} in ~25 iterations. The final T_{SD} values are used in Eq. (5) for obtaining the estimates of M.

2.2. Expression of Λ

To close the system of equations we need an expression for the evaporative fraction, Λ, and this expression must include the dependence of Λ on the conductances. For this we exploited two different representations of evaporation; the Penman (P) equation (Penman, 1948), and the Priestley–Taylor (PT) equation (Priestley & Taylor, 1972). Here, these two expressions are related to each other through the complementary relationship advection–aridity hypothesis developed by Brutsaert & Stricker (1979). According to the original complementary hypothesis (Bouchet, 1963), for a large homogeneous area of 1 to 10 km and away from sharp environmental discontinuities there exists a complementary feedback mechanism between potential evaporation (λE^*), evaporation (λE) and sensible heat flux (H). λE^* is defined as the evaporation from a wet surface under the prevailing atmospheric condition, limited only by the amount of available energy. If moisture at the surface is unlimited (i.e., when $M = 1$), $\lambda E = \lambda E^*$ and this condition is referred to as the wet-environment evaporation (λE_W). Bouchet (1963) hypothesized that under the conditions of constant energy supply to a given surface–atmosphere system, when the surface moisture becomes limited ($M \to 0$), λE falls below λE_W and some amount of energy becomes 'available'. This extra energy increases the temperature and humidity gradient of the overlying air (in the form of sensible heat or longwave back radiation) and leads to an increase in λE^* whose magnitude is equal to the decrease in λE. If moisture availability is increased, λE again starts increasing and λE^* decreases accordingly. As a result λE^* is predicated upon the prevailing moisture availability conditions. If the energy budget remains unchanged and all the excess energy is converted into sensible heat, a complementary relationship exists of the following form:

$$\lambda E + \lambda E^* = 2\lambda E_W \tag{9}$$

This feedback mechanism helps bypass the need for detailed knowledge of the complex processes and interaction between soil, vegetation, and near surface boundary layer.

Based on Bouchet's earlier work, Brutsaert & Stricker (1979) proposed an advection–aridity hypothesis that allows the formulation of λE under non-potential conditions. Their approach is based on a conceptual framework where the aridity (i.e., surface dryness) was deduced from the drying power of large scale advection as implied by the atmospheric conditions in the turbulent surface layer. According to Brutsaert & Stricker (1979), λE_W was approximated as the potential evaporation according to Priestley & Taylor (1972), λE_{PT}^*, which represents the potential evaporation under the conditions of minimal advection and λE^* was approximated as the potential evaporation according to Penman (1948), λE_P^*, in order to capture the effects of large scale advection. Therefore, any large scale advection effects causing $\lambda E_P^* > \lambda E_{PT}^*$ were assumed to be due to the regional surface moisture conditions and also due to forced convection that increases the atmospheric

vapor pressure deficit (Brutsaert & Stricker, 1979). Thus actual evapotranspiration could be computed by means of Eq. (9) assuming $\lambda E^* = \lambda E_P^*$ and $\lambda E_W = \lambda E_{PT}^*$.

$$\lambda E + \lambda E_P^* = 2\lambda E_{PT}^* \tag{10}$$

This approach was found to yield reasonable estimates of λE across both well watered and drought conditions (Brutsaert & Stricker, 1979; Huntington, Szilagyi, Tyler & Pohll, 2011; Parlange & Katul, 1992). The main advantage of this approach is that it does not require a submodel for representing the stomatal conductance, soil moisture or any other land surface measures of aridity. Taking advantage of this advection–aridity hypothesis we are able to express the evaporative fraction in terms of the two conductances (g_B and g_S) and therefore we are able to close the system of equations in the present scheme (see Section 2.3 and Appendix A).

One obvious question arises over the interdependence of the P and PT equations because the PT equation was derived from Penman's equation. According to Penman (1948), λE_P^* is written as follows.

$$\lambda E_P^* = \frac{s\Phi}{s+\gamma} + \frac{\rho c_P g_B D_A}{s+\gamma} \tag{11}$$

The first term of Eq. (11) may be considered to represent the lower limit of evaporation from a moist surface, which was referred to as 'equilibrium evaporation' by Slatyer & Mcllroy (1961) or diabatic evaporation by Penman (1948). The second term of Eq. (11) is a measure of the departure from this equilibrium state in the atmosphere and is often referred to as the adiabatic evaporation (Penman, 1948) or 'drying power' of air (Granger & Gray, 1989). In the absence of radiative divergence, this adiabatic departure would stem from large-scale advection involving horizontal variations of surface variables (e.g., T_S, soil moisture etc.) and atmospheric conditions. The atmospheric boundary layer is not uniform and tends to maintain a humidity deficit, even over the ocean. Therefore, true equilibrium conditions are rarely encountered over a wet surface. Analyzing data collected over various surfaces Priestley & Taylor (1972) proposed an empirical adjustment of the equilibrium evaporation expression,

$$\lambda E_{PT}^* = \frac{\alpha s\Phi}{s+\gamma} \tag{12}$$

where α is a compensation factor introduced due to neglecting the adiabatic term in the Penman equation. They decided that for a large saturated landscape with minimum advection the best estimate of α is 1.26 (Priestley & Taylor, 1972). Therefore, the interdependence of λE_{PT}^* and λE_P^* is not by chance. When the underlying surface is wet, the air is close to saturation and evaporation is dominated by the radiation term of the Penman equation. But, λE_{PT}^* never equals λE_P^* because of the involvement of the 'drying power' term in λE_P^*.

It should also be emphasized that although the Priestley–Taylor α is an input into our scheme, the sensitivity analysis over a large range of α value revealed that STIC is only mildly sensitive to α (see Section 4.1 and Fig. 5b).

The main restriction of Bouchet's hypothesis can be relaxed through the introduction of this advection–aridity hypothesis (Brutsaert & Stricker, 1979) that accounts for advection through the adiabatic term of λE_P^*. Under some circumstances $\lambda E_P^* > \Phi$, which is not only due to the availability of excess energy that increases λE_P^*, but also because of horizontally advected dry air which increases the 'drying power' and hence λE_P^*. The horizontal advection is pronounced when a dry front passes over a surface and increases both D_A and g_B and consequently the drying power of air, all of which are accounted for in the estimation of λE_P^* (Brutsaert & Stricker, 1979; Huntington et al., 2011; Parlange & Katul, 1992). Moving away from any idealized condition, the stronger the advection and the greater the surface dryness, the more λE differs from its equilibrium rate. Taken as a whole, these findings would suggest that the advection–aridity hypothesis is relatively robust.

According to Budyko (Budyko, Efimova, Zubenok & Strokina, 1962; see also Roderick & Farquhar, 2004), when complementarity holds, the regional evaporation rate is limited by moisture availability in arid climates and energy availability in humid climates. However, the complementary relationship allows regional λE^* to depend on regional λE in a complementary manner throughout any range of moisture and energy availability (Ramirez, Hobbins & Brown, 2005). Some theoretical arguments suggest that the hypothesis of 1:1 compensation between λE and λE^* is only partially fulfilled (Lhomme, 1997; Sugita, Usui, Tamagawa & Kaihotsu, 2001). However, more recently Ramirez et al. (2005) found observational evidence for 1:1 compensation between λE and λE^* and, therefore, we also assume perfect compensation here.

This preamble is important because Eqs. (1), (10), (11) and (12) can be combined and algebraically reorganized to give the following expression for Λ (please see Appendix A for details).

$$\Lambda = \frac{2\alpha s}{2s + \gamma\left(2 + \frac{g_B}{g_S}\right)} \tag{13}$$

2.3. The STIC closure equations

The closure equations for STIC are as follows and their derivations are detailed in Appendix A.

$$g_B = \frac{\Phi}{\rho c_P\left(\Delta T + \frac{e_S - e_A}{\gamma}\right)} \tag{14}$$

$$g_S = g_B \frac{(e_S - e_A)}{(e_S^* - e_S)} \tag{15}$$

$$\Delta T = \left(\frac{e_S - e_A}{\gamma}\right)\left(\frac{1-\Lambda}{\Lambda}\right) \tag{16}$$

$$\Lambda = \frac{2\alpha s}{2s + \gamma\left(2 + \frac{g_B}{g_S}\right)} \tag{17}$$

These four equations provide constraints for the four unknowns g_B, g_S, ΔT, and Λ. The computational diagram is given in Fig. 3. Eqs. (14)–(17) were solved to retrieve the analytical expressions of the four unobserved components.

2.4. Partitioning λE estimates

The terrestrial latent heat flux is an aggregate of both evaporation (λE_E) and transpiration (λE_T). When it rains the land surface becomes wetter and λE tends to the potential evaporation (λE^*), while surface drying after rainfall leads λE tending to the potential transpiration rate (λE_T^*) in the presence of vegetation, or zero without any vegetation. λE at any time is, therefore, some blend of these two end member conditions depending on the degree of surface moisture availability (Bosveld & Bouten, 2003; Loescher, Gholz, Jacobs & Oberbauer, 2005). Given moisture availability (M) is a STIC output, the separation of lumped λE into λE_E and λE_T was also tested.

$$\lambda E = \lambda E_E + \lambda E_T = M\lambda E^* + (1-M)\lambda E_T^* \tag{18}$$

Having recovered g_B, λE^* can be estimated according to the Penman equation (Eq. 11) and λE_T can be estimated as the residual in Eq. (18). λE_T^* can be estimated as $\lambda E_T/(1 - M)$.

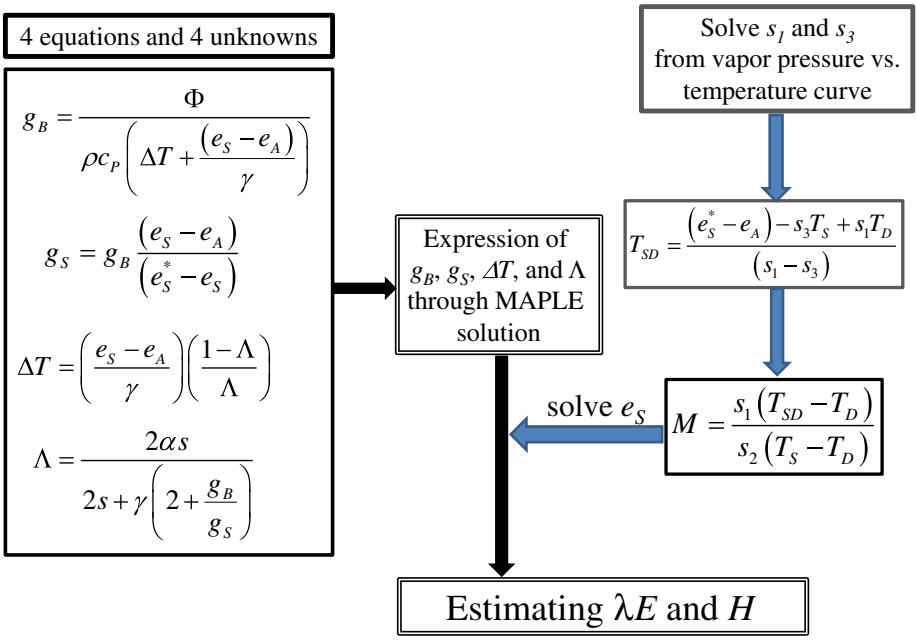

Fig. 3. Diagrammatic representation of the core equations used to recover the internal state variables in STIC. All the variables are explained in the main body of the manuscript.

3. Datasets

Estimation of λE and H through STIC requires information on R_N, G, T_A, R_H or e_A and T_S. The first four variables were available from FLUXNET sites and T_S was obtained from MODIS. Given the absence of dewpoint temperature (T_D), it was calculated from T_A and R_H according to Buck (1981) as follows.

$$T_D = \frac{c.\gamma_M(T_A, R_H)}{b - \gamma_M(T_A, R_H)} \tag{19}$$

$$\gamma_M(T_A, R_H) = \log\left(R_H \cdot \exp\left(\left(b - \frac{T_A}{d}\right)\left(\frac{T_A}{c + T_A}\right)\right)\right) \tag{20}$$

Where, b, c, and d, are empirical coefficients having values of 18.678, 257.14 and 234.5, respectively. Detailed descriptions of the different datasets are given below.

3.1. Eddy Covariance (EC) tower data (FLUXNET data)

These data include 30 EC sites covering different sub-networks of FLUXNET (Ameriflux, Euroflux, Ozfluz, FLUXNET—Canada and CarboAfrica) (Baldocchi et al., 2001) (Table 2). The data covers a broad spectrum of biomes and climate types such as the semi-arid tropics, subtropics, Mediterranean savannas, temperate grasslands, temperate forests, boreal forests and arctic wetlands. Distribution of sites (Fig. 4 and Table 2) shows that more than 50% of the total sites represent semi-arid landscapes. The main reason for selecting majority of the semi-arid sites is because these regions are characterized by strong land–atmosphere coupling (Diremeyer, Cash, Kinter, Stan, Jung, Marx, et al., 2012; Kurc & Small, 2004), which is often confounded by extreme heterogeneity in soil moisture and vegetation (Strasser & Mauser, 2001). Such features make the specifications of the surface energy balance components more sensitive to the boundary conditions. In addition, limited water resources and growing needs of urban as well as agricultural water requirements in semi-arid sites are continuously increasing the pressure on accessible groundwater and could introduce dynamical changes in the hydrological cycle (Niyogi, Kishtawal, Tripathi & Govindaraju, 2010; Pielke, Pitman, Niyogi, Mahmood, McAlpine, Hossain, et al., 2011).

EC data were obtained from the FLUXNET LaThuile database (www.fluxdata.org) and CarboAfrica network website (www.gaia.agraria.unitus.it/database/carboafrica). Independent measurements of λE and H were available along with the measurements of R_N, G, T_A and R_H. Soil moisture and precipitation data were also available through time domain reflectometer and rain gauge measurements. The energy balance closure fraction was estimated as $C_f = (\lambda E + H)/(R_N - G)$ by linear regression between the turbulent fluxes against the net available energy, forced through the origin (Barr, Morgenstern, Black, McCaughey, & Nesic, 2006). The closure fraction was found to vary from 75 to 80%. The inherent errors associated with measurements of H, λE, R_N and G using eddy covariance are reported to be 15–20% (Weaver, 1990), 15–20% (Field, Fritschen, Kanemasu, Smith, Stewart, Verma, et al., 1992), 5–10% (Twine et al., 2000) and 20–30% (Twine et al., 2000), respectively. This leaves a considerable proportion of energy unaccounted for in the partitioning of R_N to H and λE. This could lead to significant discrepancies when estimated fluxes are compared with the observations. Therefore, the measured Bowen ratio (Bowen, 1926) of the EC towers was used to adjust the measured fluxes and surface energy balance was closed as suggested by Twine et al. (2000) and later adopted by Chavez, Neale, Hipps, Prueger & Kustas (2005) and Anderson et al. (2007). For all the sites, the gap-filled half-hourly level 3 data were used. These include meteorological (T_A and R_H), micrometeorological (λE, H, R_N, and G), and associated hydrological variables (soil moisture and rainfall). The meteorological and micrometeorological data co-incident to MODIS Terra and Aqua overpass times were averaged for every eight-day (corresponding to MODIS T_S data which are eight-day products) and the eight-day data were used for running STIC. Similarly, eight-day averages of the λE and H measurements corresponding to MODIS overpass were used to validate the estimated fluxes.

3.2. MODIS data

MODIS terra has the local equatorial crossing time at approximately 10:30 AM in a descending node while Aqua has the local equatorial crossing time at approximately 1:30 PM in an ascending node with a sun-synchronous, near-polar, circular orbit. Tiles of the MODIS Terra and Aqua eight-day level-3 T_S data (MOD11A2 and MYD11A2 version 005) at 1 km spatial resolution was acquired through the Oak Ridge

Table 2
Description of the sites including latitude, longitude, biome types, climate, annual precipitation (mm) and years of data used in the study. Distribution of sites is shown in Fig. 4.

Site name	Country	Latitude	Longitude	Biome	Climate type	EC height (m)	Annual rainfall (mm)	Years	Reference
Audubon Ranch (AUD)	US	31.59	−110.51	GRA	Dry arid and Semi-arid	5	440	2002–2006	Krishnan et al. (2012)
Freeman Ranch (FR2)	US	29.95	−97.99	WSA	Subtropical Mediterranean	7	865	2004–2006	Heinsch et al. (2004)
Santarita Mesquite (SRM)	US	31.82	−110.87	WSA	Dry arid and Semi-arid	7	480	2004–2006	Scott et al. (2009)
Sky Oaks (SO2)	US	33.37	−116.62	CSH	Subtropical Mediterranean	n/a	555	2004–2006	Lipson et al. (2005)
Tonzi Ranch (TON)	US	38.43	−120.97	WSA	Subtropical Mediterranean	23	525	2002–2006	Baldocchi and Xu (2007)
Walnut Gulch (WKG)	US	31.74	−109.94	GRA	Dry arid and Semi-arid	7	410	2004–2006	Scott et al. (2010)
Flagstaff-Managed Forest (FMF)	US	35.14	−111.73	WSA	Dry arid and Semi-arid	23	625	2005–2006	Dore et al. (2010)
Flagstaff-Unmanaged Forest (FUF)	US	35.09	−111.76	WSA	Dry arid and Semi-arid	23	650	2005–2006	Dore et al. (2010)
Flagstaff-Wildfire (FWF)	US	35.45	−111.77	WSA	Dry arid and Semi-arid	23	620	2005–2006	Dore et al. (2010)
Sao Paulo Cerrado (SP1)	Brazil	−21.62	−47.65	WSA	Tropical	50	1420	2001–2002	Santos et al. (2004)
Howard Springs (HOW)	Australia	−12.49	131.15	WSA	Tropical	n/a	1450	2002–2006	Beringer et al. (2003)
Foggdam (FOG)	Australia	−12.54	131.31	WSA	Tropical	n/a	1325	2006–2007	–
Las Majadas del Tieter (LMA)	Spain	39.94	−5.77	SAV	Subtropical Mediterranean	n/a	370	2004–2006	–
Demokeya (DEM)	Sudan	13.28	30.48	GRA	Semi-arid tropics	n/a	320	2007–2009	Ardö et al. (2008)
Maun Mopane (MA1)	Botswana	−19.92	23.56	WSA	Dry arid and Semi-arid	13.5	495	2000–2001	Veenendaal et al. (2004)
Kruger National Park (KRU)	South Africa	−25.02	31.49	SAV	Subtropical Mediterranean		525	2001–2003	Williams et al. (2009)
Willow Creek (WCR)	US	45.81	−90.08	DBF	Temperate continental	30	790	2001–2006	Cook et al. (2004)
Hainich (HAI)	Germany	51.08	10.45	DBF	Temperate	42	780	2002–2006	Grünwald and Bernhofer (2007)
University of Michigan Biological Station (UMB)	US	45.56	−84.71	DBF	Temperate continental	46	805	2001–2003	Curtis et al. (2002)
Hesse forest (HES)	France	48.67	7.06	DBF	Temperate	22	795	2002–2006	Granier et al. (2000)
Cabauw (CA1)	Netherlands	51.97	4.93	GRA	Temperate	n/a	775	2003–2006	Sulkava et al. (2011)
Wetztein (WET)	Germany	50.45	11.45	ENF	Temperate	25	870	2002–2006	Rebmann et al. (2010)
Mehrstadt (MEH)	Germany	51.27	10.66	GRA	Temperate	n/a	695	2004–2006	Sulkava et al. (2011)
Grillenburg (GRI)	Germany	50.95	13.51	GRA	Temperate	5	670	2005–2005	Sulkava et al. (2011)
SSA Old Aspen (OAS)	Canada	53.63	−106.20	DBF	Boreal	n/a	430	2001–2005	Hilker et al. (2011)
Lethbridge (LET)	Canada	49.709	−112.940	GRA	Temperate	5	400	2001–2005	Flanagan et al. (2002)
Loobos (LOO)	Netherlands	52.17	5.74	ENF	Temperate	52	785	2001–2006	Sulkava et al. (2011)
Saskatchewan Fire 1977 (SF1)	Canada	53.628	−106.198	ENF	Boreal	n/a	425	2004–2005	Amiro et al. (2006)
Ontario Turkey Point Seeding White Pine (TP1)	Canada	42.661	−80.559	ENF	Boreal	10	910	2004–2005	Peichl and Arain (2006)
Ivotuk (IVO)	US	68.486	−155.75	WET	Arctic	n/a	305	2004–2006	Epstein et al. (2004)

GRA = grassland; WSA = woody savannah, SAV = savannah; CSH = closed shrubland; DBF = deciduous broadleaf forest, ENF = evergreen needleleaf forest.

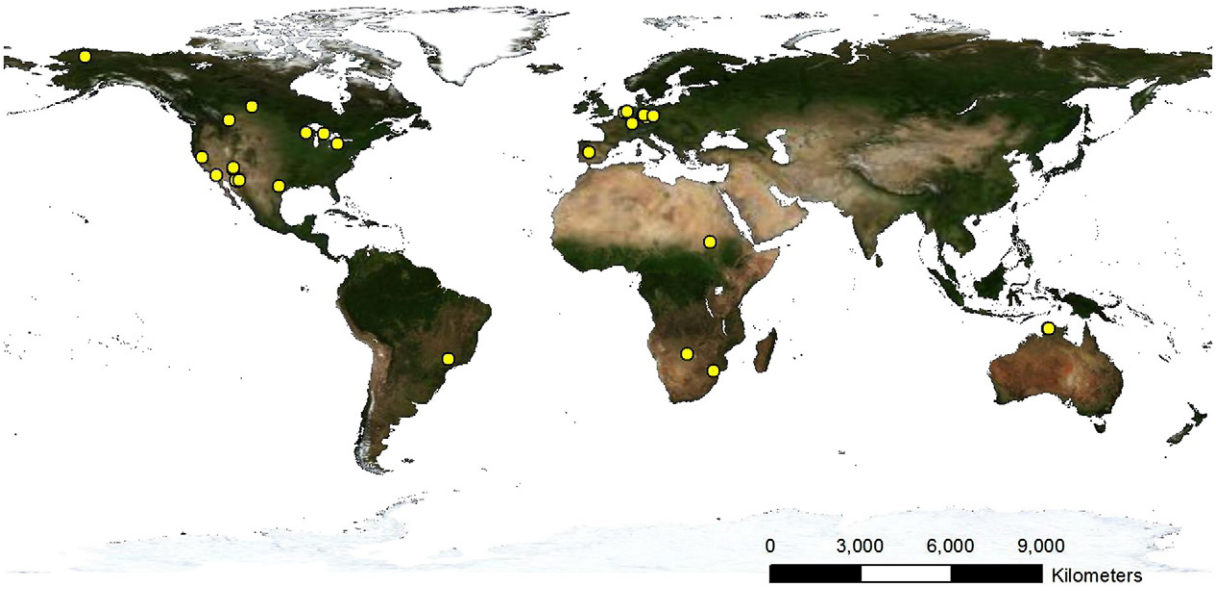

Fig. 4. Distribution of eddy covariance sites (small yellow dots) used in the present analysis spanned over different biome and climatic settings of FLUXNET covering five continents.

National Laboratory (ORNL) data gateway (http://daac.ornl.gov/MODIS/). This is the harmonized T_S data maintained by ORNL over all the flux measurement sub-networks. The data is a 7 × 7 pixel cutout centred on the EC flux measurement sites. From these cutouts, T_S of 2 × 2 pixels from the central location were again extracted and averaged. Only quality controlled data (with a QA flag of 0) were used in the pixel averaging. Any bad quality data within 2 × 2 pixels were ignored while averaging.

Despite MODIS T_S having 1 km spatial resolution and the tower meteorological variables (e.g., T_A and R_H) having a fetch <1 km, still MODIS T_S is the best available time-series data that covers multiple seasonal cycles with minimum data gaps. Similarly, FLUXNET is the best available database to estimate and validate the surface fluxes covering multiple biomes and climate regimes.

4. Results

The estimates of λ*E* and *H* made through STIC were first subjected to a sensitivity analysis, validation and a residual error analysis of the estimated λ*E*. This was followed by an evaluation of *M* and λ*E* components based on independently measured hydrological variables (soil moisture and rainfall) in the EC tower sites. Detailed evaluation of the individual conductance and ΔT is beyond the scope of this paper because no direct measurements of these variables were available.

4.1. Sensitivity analysis

The accuracy of STIC heavily depends on the quality of MODIS land surface temperature data due to its role in retrieving T_{SD} and *M*. Therefore, a sensitivity analysis of the scheme was first carried out to quantify the impacts of uncertainty in T_S on λ*E* and *H*. The nature of the sensitivity analysis used here is similar to that of Anderson et al. (1997): the absolute sensitivity (*S*) of any of the output variable (*V*) to ± X uncertainty in T_S was assigned as $S_V = \left|(V_{X_+} - V_{X_-})/V_{X_r}\right|$. Here V_{X+}, and V_{X-} are the estimated variables when the value of T_S is increased or decreased by X and V_{Xr} is the value of the estimated variable at actual T_S. Sensitivity was tested over four different biome types (cropland, grassland, savanna and forest) using actual MODIS T_S uncertainty over the North American FLUXNET sites as reported by Hulley, Hughes & Hook (2012). One representative site from each biome class was selected where the actual MODIS T_S uncertainties were 1.78 K (cropland, e.g., Bondville), 1.34 K (grassland, e.g., Walnut Gulch), 2.66 K (savanna, e.g., Freeman ranch) and 2.24 K (forest, e.g., Duke forest) (Hulley et al., 2012), respectively. Both the λ*E* and *H* were found to be sensitive to the reported T_S uncertainties with a magnitude of S_V to the order of 24–33% (for λ*E*) and 17–44% (for *H*) (Fig. 5a).

Since the Priestley–Taylor parameter (α) was involved in the entire scheme and there are reports of wide variability of α (Komatsu, 2005), the sensitivity of STIC to α was also tested for large variations in α. The reported values of α in the literature are found to vary between 1 and 1.5 (Baldocchi & Xu, 2007). Taking this range we found that for λ*E* the magnitude of S_V varied from 10 to 13% and for *H* it varied from 9 to 16% (Fig. 5b). This suggests that STIC is not particularly sensitive to α and assigning α = 1.25 does not introduce significant error in the λ*E* and *H* outputs. Maximum RMSE difference in λ*E* and *H* was 10 and 15 W m^{-2}, respectively.

Sensitivity of STIC was also tested for the atmospheric vapor pressure (e_A) and both the fluxes were not very sensitive to ± 10% uncertainty in the e_A values (Fig. 5c). The magnitude of S_V varied between 5–6% for λ*E* and 3–9% for *H*. The typical errors of water vapor retrieval from the current MODIS atmospheric data and Atmospheric Infrared Sounder (AIRS) are 5–10% (Gao & Kaufman, 2003) and 10% (Tobin, Revercomb, Knuteson, Lesht, Strow, Hannon, et al., 2006), respectively. With the advent of new sensor technology and the scheduled launch of a future geostationary interferometer sounder GEOSTAR, the water vapor retrieval error will be within 5%, which will facilitate the spatial implementation of STIC for large area mapping of surface fluxes.

4.2. Evaluation of λE and H estimates at MODIS Terra and Aqua overpass time

The predicted versus measured λ*E* and *H* show good overall agreement in all the 30 tower sites (Table 3) with a relative cumulative error $\left(\frac{\sum(observed-estimated)}{\sum observed}\right)$ in λ*E* and *H* of the order of 4% and 3% respectively. The root mean square error (RMSE) of individual sites varied between 10.70 and 59.67 W m^{-2} with measured versus predicted correlation coefficients (*r*) between 0.55 and 0.97 (Table 3). The RMSE and *r* of λ*E* from all the sites were 37.79 W m^{-2} (11% error) and 0.89 (Table 3). The performance of STIC was consistent over all sites except FOG and DEM where the RMSE was relatively higher (see

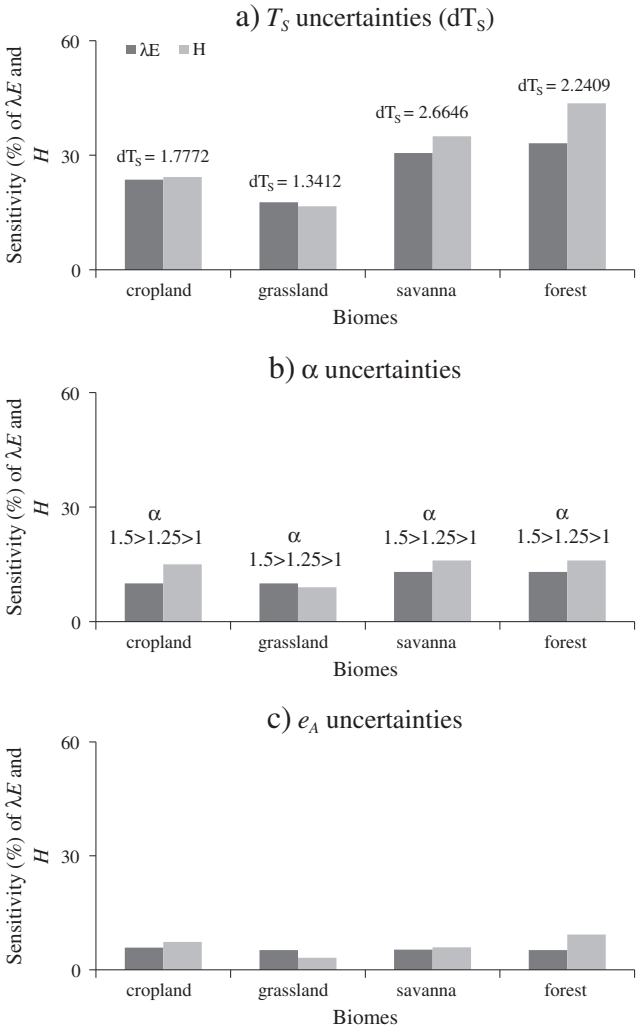

Fig. 5. Sensitivity of the STIC derived fluxes (λ*E* and *H*) to (a) actual uncertainties in MODIS Terra T_S (b) the Priestley–Taylor parameter α and (c) uncertainties in e_A over four different biomes. Actual T_S uncertainties over these biomes were obtained from Hulley et al. (2012). One representative site from every biome is chosen. The numbers of data points were 230 for cropland, 138 for grassland, 138 for forest, and 46 for savanna. Average sensitivity of all data points is reported.

Table 3). Pooled RMSE and *r* for *H* for the 30 sites were 37.74 W m^{-2} (9% error) and 0.91. RMSE's of individual sites varied between 12.11 and 58.48 W m^{-2} with *r* varying between 0.55 and 0.96 (Table 3). The pooled evaluation of λ*E* and *H* using all the tower sites revealed the credible estimates of STIC fluxes over a broad range of biomes and climatic settings. An even distribution of points around 1:1 validation line (Fig. 6a and b) indicates low bias, having a measured to predicted regression slopes of 0.99 (±0.005) and 0.88 (±0.003), respectively. Given the footprint size of one MODIS pixel is 1 km it was not possible to obtain the T_S heterogeneity within the tower footprint. However the 2 × 2 cut-out of vegetation index (i.e., NDVI) (250 m spatial resolution) around the tower sites revealed the standard deviation of NDVI to be varying from 0.01 to 0.10. Therefore, we assumed these comparisons to be reasonable although errors may be propagated due to T_S heterogeneity which is governed by the surface dryness–wetness patterns of the landscape around the EC towers, a feature not captured in NDVI data.

Consistent results are also obtained with MODIS Aqua data where the overall RMSE and *r* of the predicted λ*E* was 42.27 W m^{-2} (15% error) and 0.88 (Fig. 6c). The RMSE of individual sites varied between 26.32 and 63.77 W m^{-2} with *r* values between 0.48 and 0.90. The pooled RMSE and *r* for *H* was 44.31 W m^{-2} (8% error) and 0.90 (Fig. 6d). RMSE of individual sites varied between 23.67 and 66.65 W m^{-2} with *r* varying between 0.47 and 0.97. Fig. 6c and d showed the pooled evaluations which again indicate reasonable fits between predictions and measurements for λ*E* and *H*, having regression slopes of 0.93 (±0.006) and 0.93 (±0.005) respectively. Given MODIS Terra T_S is frequently used in the terrestrial studies (Wan, Zhang, Zhang & Li, 2004), further analyses of STIC were performed with the MODIS Terra T_S only.

Fig. 7 shows the time series comparisons between STIC fluxes and their measured FLUXNET counterparts for six different climatic groups. These reveal that the temporal dynamics of λ*E* and *H* are consistently captured by STIC throughout the entire study period. In SP1 (Fig. 7b), relatively less seasonality was found in both measured and predicted λ*E*, and almost no seasonality was found in *H*. This is because SP1 is a tropical site with an annual rainfall of 850–1100 mm evenly distributed throughout the year and T_S also showed less seasonality (with a coefficient of variation of 0.13). This combination might be responsible for lesser seasonal component of the surface fluxes in SP1.

The residual λ*E* error (predicted–observed) was negatively correlated ($r = 0.47$) with the observed λ*E* (Fig. 8a). Fig. 8a also highlights slight overestimation for the lower range of λ*E* (<50 W m^{-2}), and improvements with increasing λ*E*. This was further confirmed when the residual error was found to be negatively correlated ($r = -0.30$) with the measured surface soil moisture (θ) (Fig. 8b) and R_N/D_A ratio ($r = -0.31$) (Fig. 8c) for their lower range values (for θ = 0–10 m^3 m^{-3} and R_N/D_A = 0–25). The residual error was also positively correlated to T_S ($r = 0.13$) and D_A ($r = 0.31$) for a D_A range of 20–50 hPa (Fig. 8d, e and inset of 8e). The residual error was evenly distributed across the entire range of T_A (Fig. 8f). Like λ*E*, the residual errors in *H* were also found to be influenced by the same variables, but in the opposite direction.

4.3. Evaluation of daily λE and H estimates using MODIS Terra

Daily λ*E* was computed following the principle of diurnal conservation of evaporative fraction following Anderson et al. (2007). The estimated evaporative fraction ($\Lambda = \lambda E/\lambda E + H$) from STIC was multiplied by the daily net available energy ($\Phi = R_N - G$) which was available at each EC site. Thus daily $\lambda E = \Lambda\Phi$ and daily $H = (1 - \Lambda)\Phi$. Analysis of the daily predicted versus measured λ*E* using MODIS Terra revealed RMSE to be 5.59–34.89 W m^{-2} with *r* varying between 0.61 and 0.98 (Table 4). Overall RMSE and *r* was 15.70 W m^{-2} and 0.89, with percent error ranging from 1 to 31% (Table 4). Pooled RMSE and *r* for *H* over all the sites were 14.52 W m^{-2} (6% error) and 0.88, with a range varying from 5.64–25.72 W m^{-2} and 0.48–0.96, respectively.

4.4. Evaluation of annual λE

Given the immediate connection between ecosystem water use and water resource management (Anderson et al., 2012), annual evapotranspiration (*E*) over the flux towers was also evaluated. Annual *E* was computed by summing the eight-day λ*E* values. If in any year, observed or estimated *E* value in an eight-day block was missing, that particular year was not included in the computation. If such gaps exist for all the years in any of the study sites, that particular site was not accounted in this analysis. The analysis revealed a good agreement for all sites (Fig. 9a) with $r = 0.95$ and RMSE of 41 mm yr^{-1}. The magnitude of E_T had a wide range (Fig. 9b) between 114 and 720 mm, with a minimum E_T over the WKG and maximum E_T over FOG. STIC successfully captured this range.

4.5. Surface moisture availability (M) and partitioned λE

Fig. 10(a and b) shows the surface moisture availability (*M*) along with the partitioned λ*E* (λE_E and λE_T) for representative grassland (WKG) and savanna (HOW) sites having contrasting annual rainfall (R_F). This reveals the higher proportion of λE_E (52% of total λ*E*) in

Table 3
Error statistics of STIC derived eight-day average of MODIS Terra equatorial crossing time λ*E* and *H* over the eddy covariance sites of FLUXNET.

Site	N	λE						H					
		RMSE (W m^{-2})	MB (W m^{-2})	*r*	Mean observed λE	Mean STIC λE	Error (%)	RMSE (W m^{-2})	MB (W m^{-2})	*r*	Mean observed H	Mean STIC H	Error (%)
AUD	230	33.05	13.66	0.77	60.44	70.73	17	35.32	−13.02	0.87	183.83	169.15	8
FR2	138	33.02	27.72	0.90	122.26	153.68	26	39.07	−25.72	0.85	163.93	140.31	14
SRM	138	21.23	3.44	0.91	56.16	59.60	6	24.16	−13.63	0.95	184.73	171.10	7
SO2	138	33.86	9.26	0.55	81.91	91.19	11	40.70	−21.40	0.89	225.56	204.15	9
TON	230	40.63	13.32	0.71	72.11	86.32	20	46.84	−31.73	0.95	186.60	158.36	15
WKG	138	23.34	2.83	0.81	44.28	45.30	2	24.01	−2.52	0.93	161.03	158.00	2
FMF	92	34.88	2.27	0.85	97.87	100.14	2	35.26	−14.13	0.92	219.94	205.81	6
FUF	92	33.54	5.73	0.83	82.03	87.76	7	36.76	−16.42	0.92	231.91	215.48	7
FWF	92	20.18	3.88	0.90	67.21	71.10	6	24.43	−13.19	0.96	168.40	155.21	8
SP1	92	39.39	6.29	0.92	198.05	203.68	3	39.28	−8.09	0.72	148.60	138.41	7
HOW	230	45.76	0.34	0.79	199.01	197.58	1	41.87	−15.29	0.75	139.06	126.36	9
FOG	92	59.67	4.96	0.79	242.03	250.67	4	55.95	3.92	0.65	91.65	89.87	2
LMA	138	31.32	0.09	0.89	95.71	96.37	1	31.67	0.10	0.93	132.46	134.78	2
DEM	138	52.45	19.11	0.85	99.21	117.68	19	58.48	−35.00	0.55	204.89	169.10	17
MA1	92	44.58	35.34	0.83	86.93	126.37	45	52.47	−42.41	0.84	191.25	144.45	24
KRU	138	32.96	13.77	0.75	68.98	78.61	14	34.23	−15.56	0.82	216.84	202.75	7
WCR	276	44.24	25.23	0.90	74.22	89.15	20	44.17	−25.15	0.79	122.80	105.90	14
HAI	230	34.88	17.11	0.89	64.29	79.12	23	35.06	−17.44	0.89	97.49	86.39	11
UMB	138	31.09	11.88	0.97	99.61	114.63	15	31.19	−11.89	0.90	107.50	109.61	2
HES	230	38.81	20.69	0.89	62.93	85.96	37	40.76	−23.64	0.86	97.34	80.02	18
CA1	184	31.20	−24.27	0.96	107.30	94.56	12	32.36	24.92	0.86	55.20	74.73	35
WET	230	42.85	16.93	0.89	65.22	85.77	31	42.85	−16.93	0.91	107.69	96.04	11
MEH	138	25.49	14.64	0.96	61.13	77.70	27	26.96	−18.14	0.95	76.91	60.64	21
GRI	92	19.21	−11.87	0.97	70.47	58.24	17	18.99	11.68	0.85	39.12	41.01	5
OAS	230	32.85	12.57	0.91	54.21	67.90	25	40.71	−19.62	0.91	105.32	87.97	16
LET	230	32.34	4.39	0.90	61.37	67.87	10	33.56	−6.29	0.91	107.33	109.29	2
LOO	276	39.04	8.41	0.86	87.69	105.03	20	40.29	−12.77	0.87	108.02	90.20	17
SF1	92	31.90	11.62	0.94	74.37	84.52	14	32.40	−12.31	0.96	120.79	109.79	9
TP1	92	45.96	−35.58	0.96	152.90	117.43	23	45.13	34.64	0.85	74.09	113.65	53
IVO	138	10.70	−2.82	0.94	16.53	13.49	18	12.11	0.82	0.95	18.59	18.99	2
Pooled	4646	37.79	10.10	0.89	93.20	103.31	11	37.74	−12.18	0.91	138.52	126.34	9

HOW as compared to WKG (34% of total λ*E*). This is because the annual rainfall in HOW is nearly three times higher than the annual rainfall in WKG. This might have led to high surface wetness in HOW and as a result λE_E might have dominated. Seasonality was evident in *M*, λE_E and λE_T dynamics. λE_T was dominant particularly during the growing season while λE_E dominated immediately after the rainfall. However, there tend to be some λE_E signals even when there was no rainfall (Fig. 10). Given the MODIS Terra overpass time, the morning dew might have contributed to some degree of λE_E in the absence of rainfall. Dew is an important source of moisture in the semi-arid regions and it surrounds the surface nearly every morning for approximately two to three hours past sunrise (Baier, 1966; Malek, McCurdy & Giles, 1999). The weather data of most of the sites confirmed the differences between midnight to early morning T_A and T_D to be quite narrow, which might have developed a favorable environment for the dew formation. Over the entire time period, $\Sigma\lambda E_E/\Sigma\lambda E$ varied from 33 to 63% across all the sites (Table 5). Highest proportion (63%) of λE_E was found in the SP1 which also had the highest R_F (1420 mm) during the entire study period. The proportion of $\Sigma\lambda E_T/\Sigma\lambda E$ varied between 40 and 67% for all the sites (Table 5).

Significant correlation ($r = 0.31$–0.88) was found between *M* and the observed surface soil moisture (θ) across all the grassland and savanna sites and very low or no correlation ($r = 0.0$–0.18) was found in the forest sites (Table 5). Examples of the scatterplots between *M* and θ (Fig. 10c and d) over the representative grassland and savanna sites showed the reliability of retrieved *M* to reasonably capture the dynamics of θ over the landscapes having low or sparse vegetation cover. Table 5 also shows significant cross correlation ($r = 0.33$–0.62) between *M* and eight-day cumulative R_F for the grasslands and savannas and no or poor correlation ($r = 0.0$–0.17) over the forests.

The retrieved λE_E was significantly related to θ over almost every grassland and savanna site with *r* varying from 0.24 to 0.79 (Table 5). No relationship between λE_E and θ was found in the temperate and boreal forest sites. Examples of the scatterplots (Fig. 10e and f) between λE_E and θ over the representative grassland and savanna sites confirmed the dominance of λE_E under higher surface wetness conditions. The effects of atmospheric water demand and annual R_F were reflected in the relationships between *M*, θ, and λE_E. Regions having high D_A and low annual R_F (<500 mm) generally showed higher correlation between *M*, θ, and λE_E (Table 5). An exception was HOW, where the correlation was substantially high despite receiving very high annual R_F (1450 mm). This may be due to the existence of high atmospheric 'drying power' and strong land atmosphere interaction hot-spot over the Australia that helps maintaining such close relationship between *M*, θ, and λE_E (Koster et al., 2006), despite receiving high annual R_F.

Given the close link between transpiration and root zone soil moisture (θ_d) (Anderson et al., 2007; Guswa, 2005; Noilhan & Planton, 1989; Small & McConnell, 2008), the retrieved λE_T was also linked with the tower measured θ_d (wherever available). A significant relationship ($r = 0.30$–0.67) (Table 5) was found in the semi-arid grasslands and savannas under the conditions of moderate to high atmospheric water demand ($D_A >= 10$ hPa) (Fig. 11a and inset). But no relationship between λE_T and θ_d was apparent under low D_A ($D_A < 10$ hPa) despite the availability of unlimited radiation (R_G) and high leaf area index (L) (Fig. 11a and c). A direct response of λE_T to R_G was also evident ($r = 0.70$–0.90) when θ_d exceeded certain threshold limit (>15 m^{3}m^{-3}) (Fig. 11b). No relationship between λE_T and θ_d was found in the high latitude forests and temperate grasslands due to the low humidity deficit of air.

5. Discussion

This study has shown that the surface flux estimates from STIC are able to capture the observed dynamics of the fluxes over diverse biomes and climate types and provide reasonable estimates of λ*E* (and *H*) and its components. A systematic overestimation of λ*E* is noted when very

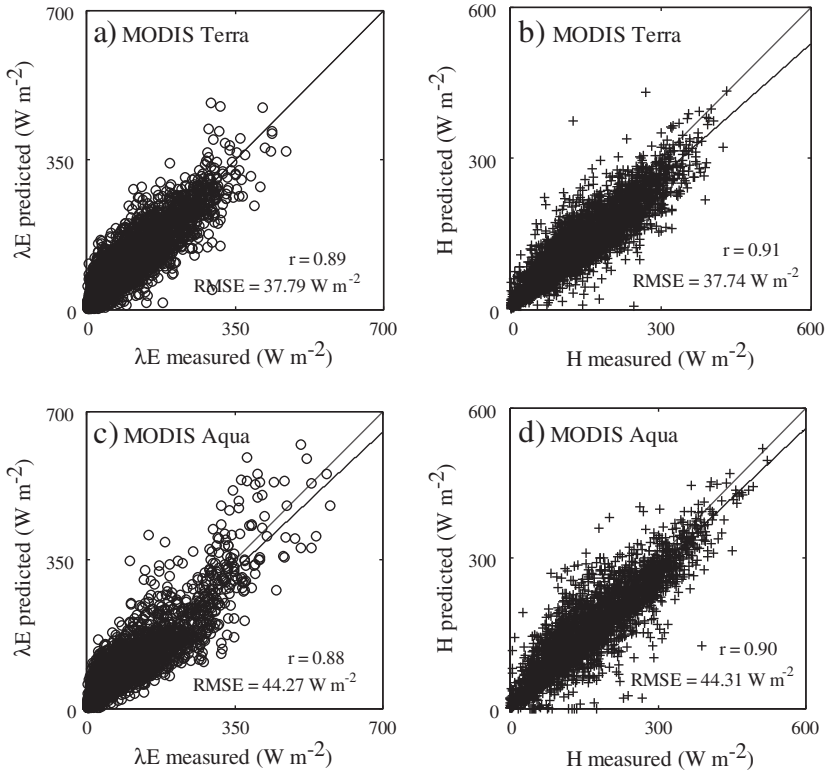

Fig. 6. Comparison of measured versus STIC estimates of (a) λE using MODIS Terra T_S and tower meteorology over the 30 EC sites of FLUXNET with $\lambda E_{predicted} = 0.99\ (\pm 0.005)\lambda E_{measured}$, (b) H using MODIS Terra T_S and tower meteorology over the 30 EC sites of FLUXNET with $H_{predicted} = 0.88(\pm 0.003)H_{measured}$, (c) λE using MODIS Aqua T_S and tower meteorology over the 28 EC sites of FLUXNET with $\lambda E_{predicted} = 0.93\ (\pm 0.006)\lambda E_{measured}$, (d) H using MODIS Aqua T_S and tower meteorology over the 28 EC sites of FLUXNET with $H_{predicted} = 0.93\ (\pm 0.005)H_{measured}$.

low surface soil moisture is combined with a very high radiative load and atmospheric water demand (see Fig. 8b and c). This is typically found in the semi-arid regions where λE is influenced by the tight coupling between R_N, D_A and soil moisture (Gu, Meyers, Pallardy, Hanson, Yang, Heuer, et al., 2006; Small & Kurc, 2003). These might also be the reasons for the relatively higher RMSE over FOG and DEM where such tight coupling tends to dominate λE. The present moisture availability retrieval scheme (Eq. 5) does not explicitly consider this coupling, thus causing an overestimation of λE under these conditions. Granger & Gray (1989) have already described a moisture availability function that accounts for the influence of R_N, D_A and λE on M. Therefore, a hybrid approach of M retrieval may be more useful in this context.

Cloudiness and the associated biased sampling of T_S by the satellite will also affect the performance of STIC. The eight-day T_S products of MODIS are, by definition, a sample of relatively cloud free conditions whilst the tower fluxes are mixtures of clear and cloudy atmospheric conditions. The mismatch in the sampling footprint between MODIS T_S and the flux tower meteorology–micrometeorology we have used will also contribute to the uncertainty of the analysis. Another source of error will be the presence of variable dry–wet patches within a MODIS pixel as well as around the flux towers (LeMone, Tewari, Chen, Alfieri, & Niyogi, 2008). For example, if more than 50% of the area falling within a 1 km MODIS pixel is predominately wet (or dry), the lumped MODIS T_S signal will be biased due the wetness (or dryness) of the landscape. The degree to which this affects the performance of STIC needs to be assessed, although it is surprising how well the scheme has performed given little is known about within footprint heterogeneity.

The performance of STIC in comparison to other approaches cannot be directly assessed without running the other models with similar datasets, which is beyond the scope of this paper. But some inferences can be drawn by comparing and contrasting the results with other studies that also used T_S observations for computing surface energy fluxes in a single-source or two-source framework. Using hourly measurements of T_S and associated meteorological–micrometeorological variables, Norman et al. (1995) reported RMSE in λE of 60 and 50 W m^{-2} with Monsoon'90 and FIFE experimental data, while the RMSE in H was 35 (Monsoon'90) and 50 W m^{-2} (FIFE), respectively. Using a single-source surface energy balance model (SEBS), Su (2002) reported RMSE of 61.34–82.79 W m^{-2} (in λE) and 28.61–36.19 W m^{-2} (in H) over semi-arid shrub and grasses. Interestingly, in all these previous studies the prediction accuracy of H was better than that for λE. We note that STIC has a lower RMSE for both λE and H even when applied to a much broader class of land surface types and with the advantage of being independent of any aerodynamic inputs (e.g., wind speed, vegetation height and surface roughness) that are typically required to model H. The use of T_S and the temperature–saturation vapor pressure slopes to estimate the near surface moisture and vapor pressure (Fig. 2) provided the information on lower boundary conditions for λE and H. Information on surface roughness are also implicit in T_S (high roughness will cause T_S to approach T_A), R_N (through albedo and surface emissivity) and G measurements that are direct inputs into STIC.

The spatial scale mismatch between satellite and tower produced varying relationship between λE_E versus θ, M versus θ, and λE_T versus θ_d among the grasslands and savannas. θ and θ_d are the point measurements whereas the satellite retrieved M are the mixed signals of the heterogeneous wetness. Over the forests, T_S signals are mainly contributed by the vegetation and less by the soil. Therefore, the information of canopy wetness and interception evaporation was dominant in the retrieved M and λE_E (Cavanaugh et al., 2011). This led to the poor relationship between M, θ, and λE_E in the forest landscapes. The proportion of λE_E appears to be little higher than λE_T, since it includes contributions from both the canopy and soil water. However, these fractions are computed at a single snapshot during the MODIS Terra equatorial crossing time and values are likely to vary at the daily time scale. Studies over Mediterranean savanna have shown the proportion of λE_E at the daily

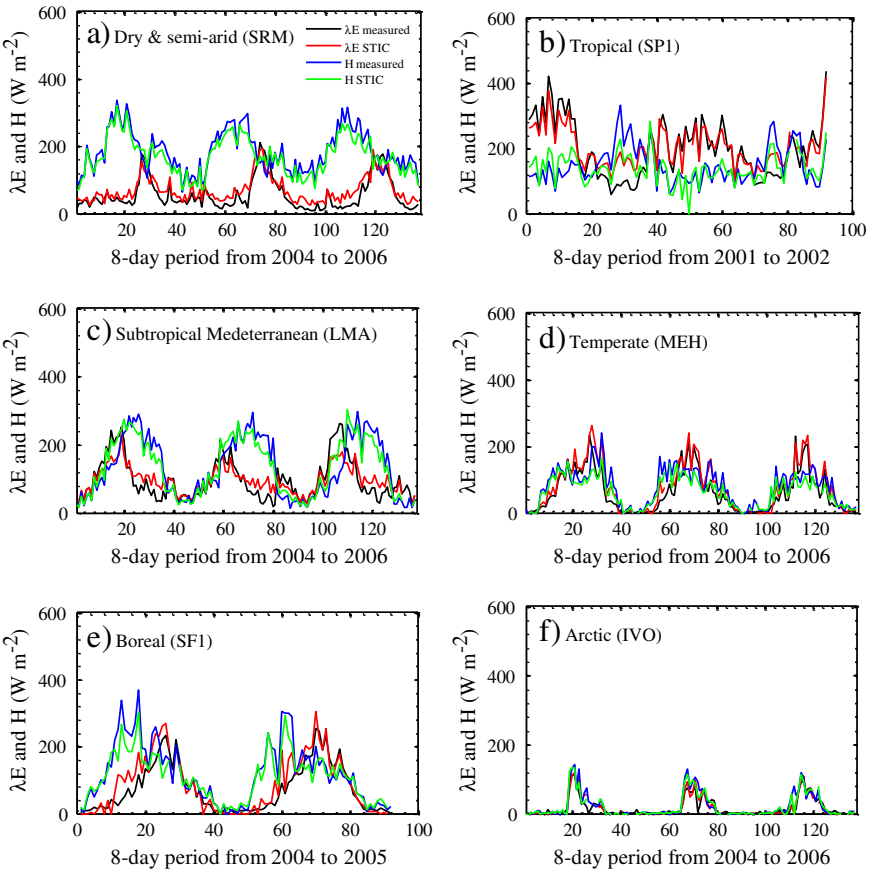

Fig. 7. Illustrative examples of the time series comparison of λ*E* and *H* observations and STIC predictions using MODIS Terra T_S and tower meteorology at selected climate types representing (a) dry & semi-arid (SRM) (b) tropical (SP1), (c) subtropical Mediterranean (LMA), (d) temperate (MEH), (e) boreal (SF1), and (f) arctic (IVO) climate group according to Koppen's climate classification. Any gap in the time series is caused either due to the absence of flux measurements or missing input data.

scale to be around 25 to 28% (Czikowsky & Fitzjarrald, 2009; David et al., 2006).

The nature of relationship between λE_T and θ_d (Table 5 and Fig. 11a) supports the hypothesis that transpiration is determined by two limiting conditions in the water-limited ecosystems: (a) uptake limited by available energy when θ_d is plentiful (Guswa, 2005), (b) by atmospheric D_A and available θ_d under water-stressed conditions (Denmead & Shaw, 1962). High D_A values result in higher soil–water content thresholds at which transpiration rates are observed to decline. The degree and the direction of the relationship between λE_T and shortwave radiation (R_G) also confirmed the fact that the energy content of the radiation absorbed by vegetation influences the transpiration (Pieruschka et al., 2010) when the level of θ_d crossed a certain limit. Even in the presence of substantial moisture in the root zone and high leaf area, λE_T may still be suppressed due to insufficient radiative load (Small & McConnell, 2008), as seen in Fig. 11b and c.

6. Conclusions and future research

The analytical method presented here addressed some of the stumbling blocks that previously hindered the direct use of radiometric surface temperature into the PM equation. This also demonstrated a physical integration of T_S and the PM equation to derive a hybrid closure that does not require the specification of surface to atmosphere conductances. An initial evaluation of STIC over a variety of biomes and climate types produced encouraging results. Errors between the predicted and observed fluxes appeared reasonable given the uncertainties in the assumptions being made and the data used. The advantage of STIC is that the Priestley–Taylor parameter, α, is the only land surface parameterizations required and STIC is relatively insensitive to the assumed value of this parameter.

The modest number of input variables required to run STIC suggests that this framework would be suitable for generating spatially explicit latent and sensible heat fields using readily available data from the current generation remote sensing platforms (e.g., MODIS and AIRS). We would also argue that because the surface conductances we produce are non-parametric byproducts of STIC, these estimates could serve as a means of developing and testing land surface parameterizations embedded within the climate and Earth system models.

We envisage further development of STIC. For example, alternative expressions to recover the surface moisture availability from the information of early morning rise in T_S (Anderson et al., 1997, 2007) or by combining R_N, D_A and T_S (Granger & Gray, 1989) needs to be explored particularly during the dry down phase. For the surface energy balance mapping with STIC at the regional and continental scale, the challenge is to obtain R_N, G, T_A and R_H or e_A that are compatible with the radiometric surface temperature data. The advent of improved thermal remote sensing data through future missions like HyspIRI, GeoSTAR and GOES-R may afford an opportunity to extend this method across multiple spatio-temporal scales, allowing for more spatially explicit hydrological and physiological process studies.

Acknowledgments

K.M. acknowledges the postdoctoral fellowship from Jet Propulsion Laboratory, California Institute of Technology under the contract of National Aeronautics and Space Administration. K.M. and A.J. was earlier supported by NERC grant (NEE0191531) during the initial development of the work. The research was initiated at Lancaster University and

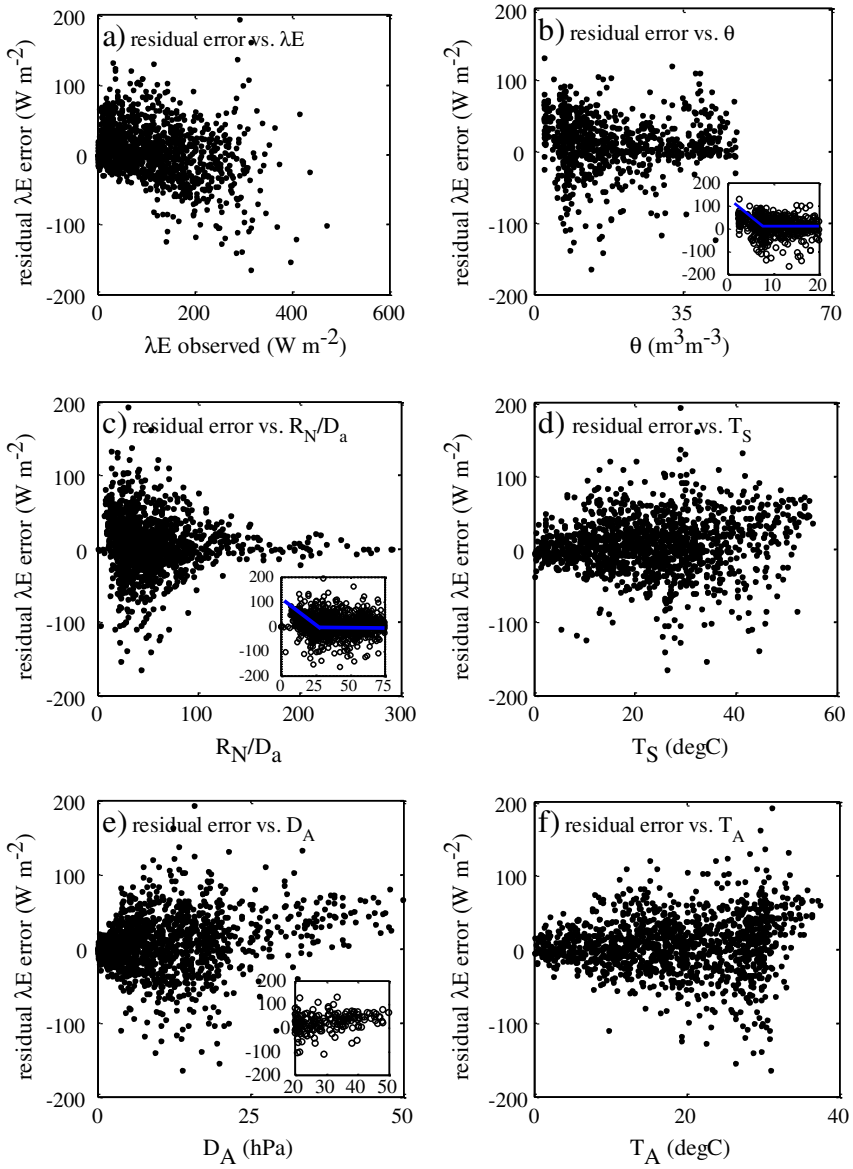

Fig. 8. Dependence of the residual error in STIC derived λ*E* on λ*E* (observed), *θ*, R_N/D_A ratio, T_S, D_A, and T_A.

completed at the Jet Propulsion Laboratory. J.B.F. was supported by JPL Research and Technology Development Grant (01STCR-R.11.118.004) and Earth System Data Record (ESDR) grant (104772-547714.04.16.01.06). We gratefully acknowledge entire FLUXNET site PIs for sharing the eddy covariance data and ORNL for maintaining the harmonized MODIS data. KM also acknowledges Dr. Junhak Lee for helping in GIS. The scientific discussions with Dr. Jozsef Szilagyi, University of Nebraska and Dr. Wilfred Brutsaert, Cornel University are also acknowledged. D.N. acknowledges partial support from NSF CAREER, NSF INTEROP, and USDA NIFA/U2U. All the copyrights of 2013 are reserved. K.M., A.J., and E.B. formulated idea, designed research and performed research; everyone contributed to writing the manuscript. The authors declare no conflict of interest.

Appendix A

Expression for g_B

The surface energy balance equation can be written as,

$$\Phi = H + \lambda E \tag{A1}$$

where Φ = net available energy ($\cong R_N - G$), H = sensible heat flux, λE = latent heat flux, R_N = net radiation, G = conductive surface heat flux or ground heat flux. All the fluxes have units in W m^{-2}.

The sensible and latent heat flux can be expressed in the form of aerodynamic transfer equations (Boegh & Soegaard, 2004; Boegh et al., 2002) as follows.

$$H = \rho c_P g_B \Delta T \tag{A2}$$

$$\lambda E = \frac{\rho c_P}{\gamma} g_B (e_S - e_A) \tag{A3}$$

In many studies ΔT is expressed as the difference between T_S and T_A ($\Delta T = T_S - T_A$) and in such cases, an 'extra conductance' is introduced to compensate for errors arising due to the inequalities between ($T_{SA} - T_A$) and ($T_{SR} - T_A$) (Boegh et al., 2002; Su, 2002). But T_S is not the true temperature that is responsible for transferring the sensible heat flux from surface to the atmosphere (Anderson et al., 1997; Norman et al., 1995; Troufleau et al., 1997). Despite the apparent simplicity of Eq. (A2), the main limitation lies in the definition of T_{SA}. T_{SA}

Table 4
Error statistics of STIC derived eight-day average λ*E* and *H* over the eddy covariance sites of FLUXNET.

Site	N	λE						H					
		RMSE (W m^{-2})	MBE (W m^{-2})	*r*	Mean observed λE	Mean STIC λE	Error (%)	RMSE (W m^{-2})	MBE (W m^{-2})	*r*	Mean observed H	Mean STIC H	Error (%)
AUD	230	11.46	0.33	0.84	21.01	22.37	6	12.65	−0.65	0.89	51.43	50.93	1
FR2	138	10.63	0.12	0.95	49.47	50.96	3	10.03	−0.38	0.81	43.90	44.94	2
SRM	138	10.39	−1.02	0.91	22.96	22.04	4	11.19	0.98	0.94	62.92	64.26	2
SO2	138	12.71	0.03	0.61	30.96	31.12	1	12.58	−0.21	0.93	71.10	71.36	0.3
TON	230	16.54	0.10	0.74	29.58	31.00	5	16.70	−0.62	0.92	58.38	59.87	3
WKG	138	9.73	0.30	0.83	17.54	16.95	3	10.03	−0.35	0.93	60.55	59.95	1
FMF	92	13.31	−5.84	0.87	35.25	29.40	17	13.89	6.03	0.93	56.78	62.62	10
FUF	92	13.23	−2.59	0.83	30.68	28.08	8	14.33	4.03	0.94	67.27	69.87	4
FWF	92	10.45	−5.69	0.89	26.27	20.57	22	10.02	5.35	0.96	40.24	45.94	14
SP1	92	14.66	−7.27	0.95	74.77	67.16	10	14.97	7.81	0.55	27.22	34.46	26
HOW	230	17.13	0.35	0.85	85.29	85.47	0.02	16.75	−0.43	0.67	49.29	47.10	4
FOG	92	26.80	−8.26	0.70	114.26	111.11	3	25.72	11.50	0.48	32.14	38.44	20
LMA	138	16.25	−7.87	0.87	40.48	32.60	19	16.43	7.32	0.89	38.34	47.43	24
DEM	138	–	–	–	–	–	–	–	–	–	–	–	–
MA1	92	13.15	8.08	0.88	30.89	40.64	31	14.77	−9.34	0.79	55.68	45.71	18
KRU	138	11.44	1.40	0.82	22.57	22.68	0.5	12.76	−1.36	0.87	61.05	57.54	6
WCR	276	15.47	−1.11	0.89	33.41	32.23	4	15.12	0.07	0.70	24.61	27.35	11
HAI	230	10.17	−0.69	0.86	24.59	22.69	8	10.23	0.21	0.86	12.65	17.71	40
UMB	138	13.55	−4.16	0.94	50.58	46.42	8	12.79	3.02	0.88	30.71	37.55	22
HES	230	12.47	0.10	0.87	21.58	22.77	6	12.54	−1.44	0.69	25.33	17.91	29
CA1	184	19.04	−17.16	0.94	40.25	27.67	31	19.40	17.31	0.62	5.77	20.41	253
WET	230	14.69	−2.53	0.82	25.97	24.89	4	14.76	1.47	0.80	15.47	25.09	62
MEH	138	5.59	−0.74	0.98	23.29	23.14	0.6	5.64	0.67	0.90	12.21	18.30	49
GRI	92	10.59	−8.63	0.96	24.59	18.74	24	10.52	8.27	0.61	3.59	12.50	248
OAS	230	16.59	−0.09	0.84	23.57	23.85	1	16.45	−0.22	0.85	36.10	30.77	15
LET	230	17.14	−6.12	0.89	24.49	20.00	18	17.50	6.00	0.74	17.89	27.62	54
LOO	276	17.74	−6.13	0.79	38.72	34.22	11	14.41	0.81	0.84	22.51	27.89	24
SF1	92	11.80	−1.79	0.92	33.81	31.77	6	11.84	1.44	0.93	30.33	37.52	24
TP1	92	34.89	−21.86	0.81	76.16	60.15	21	22.59	19.42	0.79	10.84	39.66	265
IVO	138	6.26	−2.15	0.93	9.36	5.76	38	6.22	1.70	0.93	5.66	8.56	51
Pooled	4508	15.70	−3.35	0.89	41.03	37.68	8	14.52	2.48	0.88	42.84	45.32	6

No daily data was available for DEM.

is theoretically an air temperature at the source/sink height, which is different from the physical temperature (T_S) of the surface (Monteith, 1965). It is the temperature of the thin boundary layer in the immediate vicinity of the surface level (Fig. 1) and is responsible for the transfer of heat from surface to the atmosphere. This level is defined as the source height where wind speed is zero and T_{SA} is obtained by extrapolating the logarithmic profile of T_A down to that level (Troufleau et al., 1997).

By combining Eqs. (A1), (A2) and (A3) and solving for g_B, we get

$$g_B = \frac{\Phi}{\rho c_p\left(\Delta T + \frac{(e_S - e_A)}{\gamma}\right)} \tag{A4}$$

Expression for g_S

According to Boegh et al. (2002), λ*E* can also be expressed as,

$$\lambda E = \frac{\rho c_p}{\gamma} g_S\left(e_S^* - e_S\right) \tag{A5}$$

Combining Eqs. (A3) and (A5) and solving for g_S, we can express g_S in terms of g_B, e_S^*, e_S, *and* e_A.

$$g_S = g_B \frac{(e_S - e_A)}{(e_S^* - e_S)} \tag{A6}$$

Water vapor transfer occurs from within the vegetation (transpiration) and from the immediate vicinity of the vegetation surface (evaporation). The stomatal cavities are assumed to be saturated with respect to water vapor, therefore, e_S^* of dense canopies can always be estimated from T_S. For extremely dry bare soil, the evaporating front may sometimes be located little below the dry surface layer and expressing e_S^* in terms of T_S may produce some errors under such circumstances. Recognizing the power of T_S to detect the signal of the surface as well as the subsurface dry–wet regimes (Anderson et al., 2008; Kustas & Anderson, 2009), e_S^* was estimated from T_S in the present case.

Given the measurements or estimates of e_A, e_S^*, Φ, ρ, c_p, and γ, there remain one additional unknown variable (ΔT) in Eqs. (A4) and (A6). Here we have used the Bowen ratio (β) (Bowen, 1926) equation for expressing ΔT.

Expression for ΔT

An expression for ΔT was derived from the Bowen ratio (β) equation (Bowen, 1926).

$$\beta = \gamma \frac{\Delta T}{e_S - e_A} \tag{A7}$$

Assuming closure of the surface energy balance it is possible to express β in terms of evaporative fraction (Λ) (Shuttleworth et al., 1989).

$$\beta = \frac{1-\Lambda}{\Lambda} \tag{A8}$$

Λ is defined as the fraction of available energy (Φ) partitioned towards λ*E*. Substituting for β in Eq. (A8) we get an expression for ΔT in terms of Λ.

$$\Delta T = \left(\frac{e_S - e_A}{\gamma}\right)\left(\frac{1-\Lambda}{\Lambda}\right) \tag{A9}$$

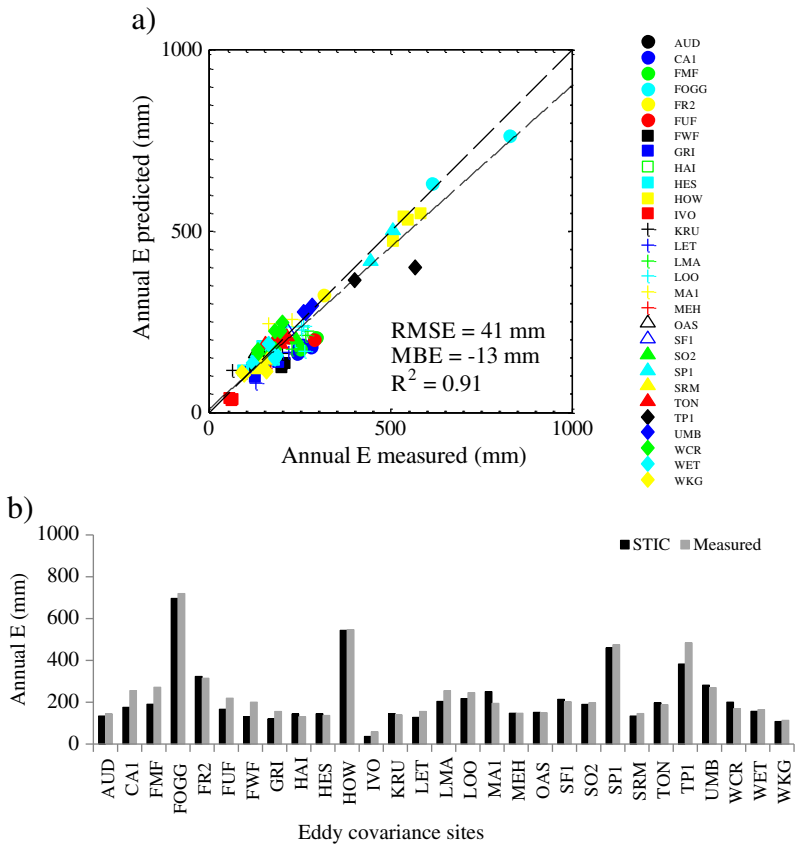

Fig. 9. (a) Validation of STIC estimates of annual E against the tower measurements. These are the annual sum of E for multiple years at each of the flux tower sites. (b) Bar chart of mean annual measured E and estimated E. Averaging all the individual year E values were done over the eddy covariance sites. The number of years in this averaging varied from at least 1 to maximum 5.

While expressing ΔT, another extra variable (Λ) is introduced in Eq. (A9). One more equation is needed to close the system of equations and this equation must introduce the dependence of Λ on the conductances. In order to express Λ in terms of g_B and g_S we had adopted the advection–aridity hypothesis (Brutsaert & Stricker, 1979).

Expression for Λ

According to Brutsaert & Stricker (1979),

$$E_P^* = 2E_{PT}^* - E \tag{A10}$$

dividing both sides by E we get,

$$\frac{E}{E_P^*} = \frac{E}{2E_{PT}^* - E} \tag{A11}$$

and dividing the numerator and denominator of the right hand side of Eq. (A11) by E_{PT}^* we get,

$$\frac{E}{E_P^*} = \frac{\frac{E}{E_{PT}^*}}{2 - \frac{E}{E_{PT}^*}} \tag{A12}$$

Expressing Φ as $\Phi = E/\Lambda$ gives,

$$\frac{E}{E_{PT}^*} = \frac{\Delta + \gamma}{\alpha s}\Lambda \tag{A13}$$

Now substituting E/E_{PT}^* from Eq. (A13) into Eq. (A12) and after some algebra gives

$$\frac{E}{E_P^*} = \frac{\Lambda(s+\gamma)}{2\alpha s - \Lambda(s+\gamma)} \tag{A14}$$

According to the Penman equation (Penman, 1948) and PM equation (Monteith, 1965),

$$\frac{E}{E_P^*} = \frac{\frac{s\Phi + \rho c_P g_B D_A}{s + \gamma\left(1 + \frac{g_B}{g_S}\right)}}{\frac{s\Phi + \rho c_P g_B D_A}{s+\gamma}} = \frac{s+\gamma}{s + \gamma\left(1 + \frac{g_B}{g_S}\right)} \tag{A15}$$

Equating Eqs. (A14) and (A15) gives an expression for Λ in terms of the conductances,

$$\frac{\Lambda(s+\gamma)}{2\alpha s - \Lambda(s+\gamma)} = \frac{s+\gamma}{s + \gamma\left(1 + \frac{g_B}{g_S}\right)}$$

which, after some algebra, gives the final expression of Λ in terms of g_B and g_S.

$$\Lambda = \frac{2\alpha s}{2s + \gamma\left(2 + \frac{g_B}{g_S}\right)} \tag{A16}$$

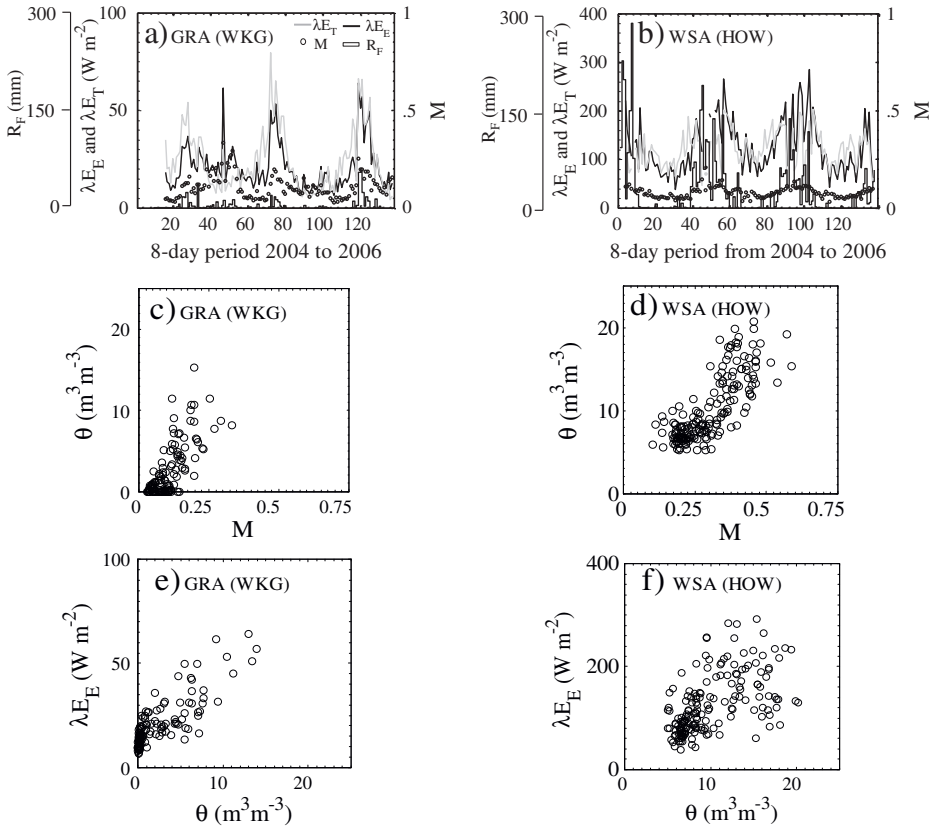

Fig. 10. (a) Estimates of the evaporation (λE_E) (thick black line) and transpiration (λE_T) (thick grey line) components of λE along with the surface moisture availability (M) (black dots) and rainfall (R_F) (bar) for representative sites of grassland (WKG) and (b) woody savanna (HOW). These two sites has contrasting annual R_F pattern. (c) and (d) Two dimensional scatters between retrieved M (black dots) with the tower measured upper layer soil moisture (θ) for similar representative grassland (WKG) and woody savanna (HOW) sites. (e) and (f) Illustrative examples of the two dimensional scatter between retrieved λE_E and tower measured θ in grassland (WKG) and woody savanna (HOW).

Table 5
Proportion of $\mathbf{\lambda E_E}$ and $\mathbf{\lambda E_T}$ from STIC over all the sites along with the cross correlation between M vs. θ, $\mathbf{\lambda E_E}$ vs. θ, $\mathbf{\lambda E_T}$ vs. θ_d, and M vs. R_F.

Biome	Site name	$\Sigma\lambda E_E/\Sigma\lambda E$	$\Sigma\lambda E_T/\Sigma\lambda E$	Correlation (M vs. θ)	Correlation (M vs. R_F)	Correlation (λE_E vs. θ)	Correlation (λE_T vs. θ_d)
Grassland, shrubland, savanna	AUD	0.40	0.60	0.48	0.39	0.43	0.50
	FR2	0.43	0.57	0.55	0.45	0.24	n/a
	SRM	0.34	0.66	0.76	0.47	0.69	0.33
	SO2	0.47	0.53	0.72	0.60	0.39	0.30
	TON	0.43	0.57	0.76	0.53	0.58	0.67
	WKG	0.34	0.66	0.76	0.47	0.79	0.62
	FMF	0.50	0.50	n/a	0.48	n/a	n/a
	FUF	0.52	0.48	n/a	0.33	n/a	n/a
	FWF	0.50	0.50	n/a	0.30	n/a	n/a
	SP1	0.63	0.37	0.31	0.47	0.38	0.54
	HOW	0.52	0.48	0.78	0.62	0.53	n/a
	FOG	0.35	0.65	n/a	0.41	n/a	n/a
	LMA	0.51	0.49	0.63	0.37	0.50	0.34
	DEM	0.33	0.67	0.88	0.37	0.51	0.66
	MA1	0.45	0.55	0.58	0.38	0.53	0.45
	KRU	0.37	0.66	0.55	0.45	0.44	0.37
	CA1	0.58	0.42	n/a	0.18	0.0	n/a
	MEH	0.62	0.43	0.42	0.17	0.40	0.0
	GRI	0.61	0.43	n/a	0.15	n/a	n/a
	LET	0.44	0.60	n/a	n/a	n/a	n/a
Forests	WCR	0.55	0.47	0.0	0.0	0.11	0.06
	HAI	0.61	0.41	0.17	0.15	0.0	0.0
	UMB	0.51	0.49	n/a	n/a	n/a	n/a
	HES	0.56	0.44	0.11	0.12	0.0	0.0
	WET	0.60	0.40	0.14	0.16	0.0	0.0
	OAS	0.58	0.48	0.0	0.10	0.11	0.10
	LOO	0.57	0.44	0.18	0.17	0.0	0.0
	SF1	0.63	0.44	n/a	n/a	n/a	n/a
	TP1	0.55	0.51	n/a	0.14	n/a	n/a
	IVO	0.60	0.52	n/a	n/a	n/a	n/a

n/a: no or spurious measurements of both θ and θ_d were available in these sites; This analysis is done with the MODIS Terra data only.

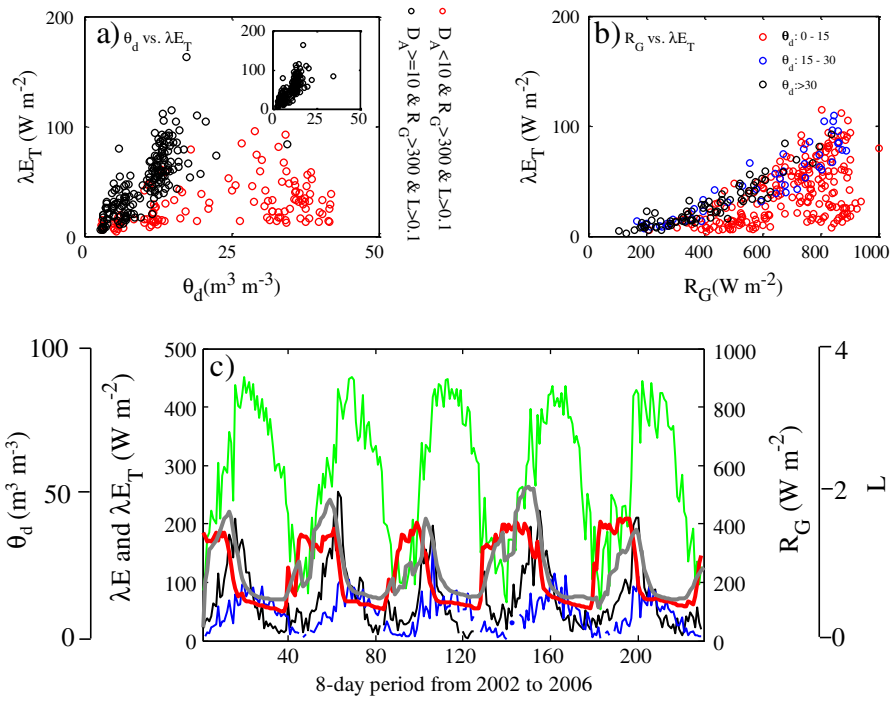

Fig. 11. Examples of the scatterplot between (a) retrieved transpiration (λE_T) versus measured root zone soil moisture (θ_d) over semi-arid savanna for two different combinations of D_A, shortwave radiation (R_G) and leaf area index (L). The figure in the inset shows good correspondence between λE_T and θ_d when D_A goes above 10 hPa, (b) λE_T versus R_G for different levels of θ_d, (c) the temporal dynamics of λE_T (blue line) along with the observed λE (black line), R_G (green line), MODIS leaf area index (L) (thick red line) and θ_d (thick grey line) over TON. This shows that λE_T has a direct response to R_G, but λE_T does not respond immediately with increase in θ_d unless D_A rises above some level.

There are many discussions on the usefulness of Brutsaert & Stricker (1979) approach and its appropriate scale of applicability. It should be noted that the advection–aridity hypothesis leads to an assumed link between g_B and radiometric surface temperature (T_S). Therefore, the effects of advection and surface moisture are implicit (although not explicit) in the advection–aridity equation.

References

Amiro, B.D., Orchansky, A. L., Barr, A. G., Black, T. A., Chambers, S. D., Chapin, F. S., et al. (2006). The effect of post-fire stand age on the boreal forest energy balance. *Agricultural and Forest Meteorology*, *140*, 41–50.

Anderson, M. C., Allen, R. G., Morse, A., & Kustas, W. P. (2012). Use of Landsat thermal imagery in monitoring evapotranspiration and managing water resources. *Remote Sensing of Environment*, *122*, 50–65.

Anderson, M. C., Norman, J. M., Diak, G. R., Kustas, W. P., & Mecikalski, J. R. (1997). A two-source time-integrated model for estimating surface fluxes using thermal infrared remote sensing. *Remote Sensing Environment*, *60*, 195–216.

Anderson, M. C., Norman, J. M., Kustas, W. P., Houborg, R., Starks, P. J., & Agam, N. (2008). A thermal-based remote sensing technique for routine mapping of land-surface carbon, water and energy fluxes from field to regional scales. *Remote Sensing Environment*, *112*, 4227–4241.

Anderson, M. C., Norman, J. M., Mecikalski, J. R., Otkin, J. A., & Kustas, W. P. (2007). A climatological study of evapotranspiration and moisture stress across the continental United States based on thermal remote sensing. 1: Model formulation. *Journal of Geophysical Research*, *112*(D10117), 1–17.

Ardö, J., Mölder, M., El-Tahir, B.A., & Elkhidir, H. A.M. (2008). Seasonal variation of carbon fluxes in semi-arid Sudan. *Carbon Balance and Management*, 3(7). http://dx.doi.org/10.1186/1750-0680-3-7.

Baier, W. (1966). Studies on dew formation under semi-arid conditions. *Agricultural Meteorology*, *3*, 103–112.

Baldocchi, D.D., Falge, E., Gu, L., Olson, R., Hollinger, D., Running, S., et al. (2001). Fluxnet: a new tool to study the temporal and spatial variability of ecosystem-scale carbon dioxide, water vapor, and energy flux densities. *Bulletin of the American Meteorological Society*, *82*(11), 2415–3434.

Baldocchi, D.D., & Xu, L. (2007). What limits evaporation from Mediterranean oak woodlands—The supply of moisture in the soil, physiological control by plants or the demand by the atmosphere? *Advances in Water Resources*, *30*, 2113–2122.

Ball, J. T., Woodrow, I. E., & Berry, J. A. (1987). A model predicting stomatal conductance and its contribution to the control of photosynthesis under different environmental conditions. In J. Biggins, M. Nijhoff, & Dordrecht (Eds.), *Progress in photosynthesis research*, *4*. (pp. 5.221–5.224)Dordrecht, The Netherlands: Martinus-Nijhoff Publishers.

Barr, A. G., Morgenstern, K., Black, T. A., McCaughey, J. H., & Nesic, Z. (2006). Surface energy balance closure by the eddy covariance method above three boreal forest stands and implications for the measurement of the CO2 flux. *Agricultural and Forest Meteorology*, *140*, 322–337.

Bastiaansssen, W. G. M., Menenti, M., Feddes, R. A., & Holtslag, A. A.M. (1998). A remote sensing surface energy balance algorithm for land (SEBAL) 1. Formulation. *Journal of Hydrology*, *212–213*, 198–212.

Beringer, J., Hutley, L. B., Tapper, N. J., Coutts, A., Kerley, A., & O'Grady, A. P. (2003). Fire impacts on surface heat, moisture and carbon fluxes from a tropical savanna in north Australia. *International Journal of Wildland Fire*, *12*, 333–340.

Boegh, E., & Soegaard, H. (2004). Remote sensing based estimation of evapotranspiration rates. *International Journal of Remote Sensing*, *25*(13), 2535–2551.

Boegh, E., Soegaard, H., & Thomsen, A. (2002). Evaluating evapotranspiration rates and surface conditions using Landsat TM to estimate atmospheric resistance and surface resistance. *Remote Sensing of Environment*, *79*, 329–343.

Bosveld, F. C., & Bouten, W. (2003). Evaluating a model of evaporation and transpiration with observations in a partially wet Douglas-fir forest. *Boundary Layer Meteorology*, *108*, 365–396.

Bouchet, R. J. (1963). Evapotranspiration re'elle evapotranspiration potentielle, signification climatique. *International Association of Scientific Hydrology, General Assembly of Berkeley. Transactions, vol. 2*. (pp. 134–142). Berkeley, California: Evaporation.

Bowen, I. S. (1926). The ratio of heat losses by conduction and by evaporation from any water surface. *Physics Review*, *27*, 779–787.

Brutsaert, W., & Stricker, H. (1979). An advection–aridity approach to estimate actual regional evapotranspiration. *Water Resources Research*, *15*(2), 443–450.

Buck, A. L. (1981). New equations for computing vapor pressure and enhancement factor. *Journal of Applied Meteorology*, *20*, 1527–1532.

Budyko, M. I., Efimova, N. A., Zubenok, L. I., & Strokina, L. A. (1962). The heat balance of the earth's surface. *Izvestya Akademii Nauk SSSR. Seriya Geograficheskaya*, *1*, 6–16.

Cavanaugh, M. L., Kurc, S. A., & Scott, R. L. (2011). Evapotranspiration partitioning in semiarid shrubland ecosystems: A two-site evaluation of soil moisture control on transpiration. *Ecohydrology*, *4*(5), 671–681.

Chavez, J. L., Neale, C. M. U., Hipps, L. E., Prueger, J. H., & Kustas, W. P. (2005). Comparing aircraft-based remotely sensed senergy balance fluxes with eddy covariance tower data using heat flux source area functions. *Journal of Hydrometeorology*, *6*, 923–940.

Choudhury, B. J. (1997). Global pattern of potential evaporation calculated from the Penman–Monteith equation using satellite and assimilated data. *Remote Sensing of Environment*, *61*, 64–81.

Cleugh, H. A., Leuning, R., Mu, Q., & Running, S. W. (2007). Regional evaporation estimates from flux tower and MODIS satellite data. *Remote Sensing of Environment*, *106*, 285–304.

Cook, B.D., Davis, K. J., Wang, W. G., Desai, A., Berger, B. W., Teclaw, R. M., et al. (2004). Carbon exchange and venting anomalies in an upland deciduous forest in northern Wisconsin, USA. *Agricultural and Forest Meteorology*, *126*, 271–295.

Curtis, P.S., Hanson, P. J., Bolstad, P., Barford, C., Randolph, J. C., Schmid, H. P., et al. (2002). Biometric and eddy-covariance based estimates of annual carbon storage in five eastern North American deciduous forests. *Agricultural and Forest Meteorology*, *113*, 3–19.

Czikowsky, M. J., & Fitzjarrald, D. R. (2009). Detecting rainfall interception in an Amazonian rain forest with eddy flux measurements. *Journal of Hydrology*, *377*, 92–105.

David, T. S., Gash, J. H. C., Valente, F., Pereira, J. S., Ferreira, M. I., & David, J. S. (2006). Rainfall interception by an isolated evergreen oak tree in a Mediterranean savannah. *Hydrological Processes*, *20*, 2713–2726.

Denmead, O. T., & Shaw, R. H. (1962). Availability of soil water to plants as affected by soil moisture content and meteorological conditions. *Agronomy Journal*, *54*, 385–390.

Dewar, R. C. (1995). Interpretation of an empirical model for stomatal conductance in terms of guard cell function. *Plant Cell and Environment*, *18*(4), 365–372.

Diremeyer, P. A., Cash, B., Kinter, J. L., Stan, C., Jung, T., Marx, L., et al. (2012). Evidence for enhanced land–atmosphere feedback in a warming climate. *Journal of Hydrometeorology*, *13*, 981–995.

Dore, S., Kolb, T. E., Montes-Helu, M., Eckert, S. E., Sullivan, B. W., Hungate, B.A., et al. (2010). Carbon and water fluxes from ponderosa pine forests disturbed by wildfire and thinning. *Ecological Applications*, *20*(3), 663–683. http://dx.doi.org/10.1890/09-0934.1.

Droogers, P., & Allen, R. G. (2002). Estimating reference evapotranspiration under inaccurate data conditions. *Irrigation and Drainage Systems*, *16*, 33–45.

Entekhabi, D., Asrar, G. R., Betts, A. K., Beven, K. J., Bras, R. L., Duffy, C. J., et al. (1999). An Agenda for land-surface hydrology research and a call for the second International Hydrological Decade. *Bulletin of the American Meteorological Society*, *80*(10), 2043–2058.

Epstein, H. E., Calef, M. P., Walker, M.D., Chapin, F. S., & Starfield, A.M. (2004). Detecting changes in arctic tundra plant communities in response to warming over decadal time scales. *Global Change Biology*, *10*(8), 1325–1334.

Eslamian, S. S., Gohari, S. A., Zareian, M. J., & Firoozfar, A. (2012). Estimating Penman–Monteith reference evapotranspiration using artificial neural networks and genetic algorithm: a case study. *Arabian Journal for Science and Engineering*, *37*(4), 935–944.

Field, R. T., Fritschen, L. J., Kanemasu, E. T., Smith, E. A., Stewart, J. B., Verma, S. B., et al. (1992). Calibration, comparison, and correction of net radiometer instruments used during FIFE. *Journal of Geophysical Research*, *97*(D17), 18681–18695.

Fisher, J. B., Tu, K. P., & Baldocchi, D.D. (2008). Global estimates of the land–atmosphere water flux based on monthly AVHRR and ISLSCP-II data, validated at 16 FLUXNET sites. *Remote Sensing of Environment*, *112*(3), 901–919.

Flanagan, L. B., Wever, L. A., & Carlson, P. J. (2002). Seasonal and interannual variation in carbon dioxide exchange and carbon balance in a northern temperate grassland. *Global Change Biology*, *8*, 599–615.

French, A. N., Schmugge, T. J., Kustas, W. P., Brubaker, K. L., & Prueger, J. (2003). Surface energy fluxes over El Reno, Oklahoma, using high resolution remotely sensed data. *Water Resources Research*, *39*(6), 1164. http://dx.doi.org/10.1029/2002WR001734.

Gao, B. -C., & Kaufman, Y. J. (2003). Water vapor retrievals using Moderate Resolution Imaging Spectroradiometer (MODIS) near-infrared channels. *Journal of Geophysical Research*, *108*(D13), 4389. http://dx.doi.org/10.1029/2002JD003023.

Granger, R. J., & Gray, D.M. (1989). Evaporation from natural nonsaturated surfaces. *Journal of Hydrology*, *111*, 21–29.

Granier, A., Biron, P., & Lemoine, D. (2000). Water balance, transpiration and canopy conductance in two beech stands. *Agricultural and Forest Meteorology*, *100*, 291–308.

Grünwald, T., & Bernhofer, C. (2007). A decade of carbon, water and energy flux measurements of an old spruce forest at the Anchor Station, Tharandt. *Tellus*, *59B*, 387–396.

Gu, L., Meyers, T., Pallardy, S. G., Hanson, P. J., Yang, B., Heuer, M., et al. (2006). Direct and indirect effects of atmospheric conditions and soil moisture on surface energy partitioning revealed by a prolonged drought at a temperate forest site. *Journal of Geophysical research*, *111*, D16102. http://dx.doi.org/10.1029/2006JD007161.

Guswa, A. J. (2005). Soil-moisture limits on plant uptake: An upscaled relationship for water-limited ecosystems. *Advances in Water Resources*, *28*, 543–552.

Hall, F. G., Huemmrich, K. F., Goetz, S. J., Sellers, P. J., & Nickeson, J. E. (1992). Satellite remote sensing of surface energy balance: success, failures and unresolved issues in FIFE. *Journal of Geophysical Research*, *97*, 19061–19089.

Heinsch, F. A., Heilman, J. L., McInnes, K. J., Cobos, D. R., Zuberer, D. A., & Roelke, D. L. (2004). Carbon dioxide exchange in a high marsh on the Texas Gulf Coast: Effects of freshwater availability. *Agricultural and Forest Meteorology*, *125*, 159–172.

Hilker, T., Gitelson, A., Coops, N. C., Hall, F. G., & Black, A. T. (2011). Tracking plant physiological properties from multi-angular tower-based remote sensing. *Oecologia*, *165*(4), 865–876.

Hulley, G. C., Hughes, T., & Hook, S. J. (2012). Quantifying uncertainties in land surface temperature (LST) and emissivity retrievals from ASTER and MODIS thermal infrared data. *Geophysical Research Letter*, *117*, D23113. http://dx.doi.org/10.1029/2012JD018506.

Huntington, J. L., Szilagyi, J., Tyler, S., & Pohll, G. (2011). Evaluating the complementary relationship for estimating evapotranspiration from arid shrublands. *Water Resources Research*, *47*, W05533. http://dx.doi.org/10.1029/2010WR009874.

Jarvis, P. G. (1976). The interpretation of leaf water potential and stomatal conductance found in canopies in the field. *Philosophical Transactions of the Royal Society London, Series B*, *273*, 593–610.

Katul, G. G., Manzoni, S., Palmroth, S., & Oren, R. (2010). A stomatal optimization theory to describe the effects of atmospheric CO2 on leaf photosynthesis and transpiration. *Annals of Botany*, *105*(3), 431–442.

Komatsu, H. (2005). Forest categorization according to dry-canopy evaporation rates in the growing season: comparison of the Priestley–Taylor coefficient values from various observation sites. *Hydrological Processes*, *19*, 3873–3896.

Koster, R. D., et al. (2006). GLACE: The global land–atmosphere coupling experiment. Part I: overview. *Journal of Hydrometeorology*, *7*, 590–610.

Krishnan, P., Meyers, T. P., Scott, R. L., Kennedy, L., & Heuer, M. (2012). Energy exchange and evapotranspiration over two temperate semi-arid grasslands in North America. *Agricultural and Forest Meteorology*, *153*, 31–44.

Kurc, S. A., & Small, E. E. (2004). Dynamics of evapotranspiration in semiarid grassland and shrubland ecosystems during summer monsoon season, central New Mexico. *Water Resources Research*, *40*. http://dx.doi.org/10.1029/2004WR003068.

Kustas, W. P., & Anderson, M. C. (2009). Advances in thermal infrared remote sensing for land surface modeling. *Agricultural and Forest Meteorology*, *149*, 2071–2081.

Kustas, W. P., & Norman, J. M. (1999). Evaluation of soil and vegetation heat flux predictions using simple two-source model with radiometric temperature for partial canopy cover. *Agricultural and Forest Meteorology*, *94*, 13–29.

Landsberg, J. J., Kaufman, M. R., Binkeley, D., Isebrands, J., & Jarvis, P. G. (1991). Evaluating progress towards closed forest models based on fluxes of carbon, water and nutrients. *Tree Physiology*, *9*, 1–15.

Lee, T. J., & Pielke, R. (1992). Estimating the soil surface specific humidity. *Journal of Applied Meteorology*, *31*, 480–484.

LeMone, M.A., Tewari, M., Chen, F., Alfieri, J. G., & Niyogi, D. (2008). Evaluation of the Noah Land Surface Model using data from a Fair-Weather IHOP_2002 day with heterogeneous surface fluxes. *Monthly Weather Review*, *136*, 4915–4941.

Leuning, R. (1995). A critical appraisal of a combined stomatal–photosynthesis model for c3 plants. *Plant, Cell and Environment*, *18*, 339–355.

Lhomme, J. P. (1997). A theoretical basis for the Priestley–Taylor coefficient. *Boundary Layer Meteorology*, *82*, 179–191.

Lipson, D. A., Wilson, R. F., & Oechel, W. C. (2005). Effects of elevated atmospheric CO2 on soil microbial biomass, activity, and diversity in a chaparral ecosystem. *Applied and Environmental Microbiology*, *71*(12), 8573–8580.

Liu, S., Lu, L., Mao, D., & Jia, L. (2007). Evaluating parameterizations of aerodynamic resistance to heat transfer using field measurements. *Hydrology and Earth Systems Sciences*, *11*, 769–783.

Loescher, H. W., Gholz, H. L., Jacobs, J. M., & Oberbauer, S. F. (2005). Energy dynamics and modeled evapotranspiration from a wet tropical forest in Costa Rica. *Journal of Hydrology*, *315*, 274–294.

Malek, E., McCurdy, G., & Giles, B. (1999). Dew contribution to the annual water balances in semi-arid desert valleys. *Journal of Arid Environment*, *42*, 71–80.

Mallick, K., Jarvis, A., Fisher, J. B., Tu, K. P., Boegh, E., & Niyogi, D. (2013). Latent heat flux and canopy conductance based on Penman–Monteith and Bouchet's complementary hypothesis. *Journal of Hydrometeorology*, *14*, 419–442.

Monteith, J. L. (1965). Evaporation and environment. In G. E. Fogg (Ed.), *Symposium of the Society for Experimental Biology. The State and Movement of Water in Living Organisms*, *19*. (pp. 205–234). NY: Academic Press, Inc.

Moran, M. S., Rahman, A. F., Washburne, J. C., Goodrich, D. C., Weltz, M.A., & Kustas, W. P. (1996). Combining the Penman–Monteith equation with measurements of surface temperature and reflectance to estimate evaporation rates of semiarid grassland. *Agricultural and Forest Meteorology*, *80*, 87–109.

Mu, Q., Heinsch, F. A., Zhao, M., & Running, S. W. (2007). Development of a global evapotranspiration algorithm based on MODIS and global meteorology data. *Remote Sensing of Environment*, *111*, 519–536.

Niyogi, D., Kishtawal, C., Tripathi, S., & Govindaraju, R. S. (2010). Observational evidence that agricultural intensification and land use change may be reducing the Indian summer monsoon rainfall. *Water Resources Research*, *46*, W03533. http://dx.doi.org/10.1029/2008WR007082.

Noilhan, J., & Planton, S. (1989). A simple parameterization of land surface processes for meteorological models. *Monthly Weather Review*, *117*, 536–549.

Norman, J. M., Kustas, W. P., & Humes, K. S. (1995). A two-source approach for estimating soil and vegetation energy fluxes in observations of directional radiometric surface temperature. *Agricultural and Forest Meteorology*, *77*, 263–293.

Parlange, M. B., & Katul, G. G. (1992). An advection–aridity evaporation model. *Water Resources Research*, *28*(1), 127–132.

Peichl, M., & Arain, M.A. (2006). Above and belowground ecosystem biomass and carbon pools in an age-sequence of white pine plantations in southern Ontario, Canada. *Agricultural and Forest Meteorology*, *140*, 51–63.

Penman, H. L. (1948). Natural evaporation from open water, bare soil, and grass. *Proceedings of Royal Society London*, *A193*, 120–146.

Pielke, R. A., Pitman, A., Niyogi, D., Mahmood, R., McAlpine, C., Hossain, F., et al. (2011). Land use/land cover changes and climate: Modeling analysis and observational evidence. *Wiley Interdisciplinary Reviews: Climate Change*. http://dx.doi.org/10.1002/wcc.144.

Pieruschka, R., Huber, G., & Berry, J. (2010). Controll of transpiration by radiation. *Proceeding of the National Academy of the Sciences USA*, *107*, 13372–13377.

Priestley, C. H. B., & Taylor, R. J. (1972). On the assessment of surface heat flux and evaporation using large scale parameters. *Monthly Weather Review*, *100*, 81–92.

Ramirez, J. A., Hobbins, M. T., & Brown, T. C. (2005). Observational evidence of the complementary relationship in regional evaporation lends strong support for Bouchet's hypothesis. *Geophysical Research Letters*, *32*, L15401. http://dx.doi.org/10.1029/2005GL023549.

Raupach, M. R., & Finnigan, J. J. (1995). Scale issues in boundary-layer meteorology: Surface energy balance in heterogeneous terrain. *Hydrological Processes*, *9*, 589–612.

Rebmann, C., Zeri, M., Lasslop, G., Mund, M., Kolle, O., Schulze, E. D., et al. (2010). Treatment and assessment of the CO2-exchange at a complex forest site in Thuringia, Germany. *Agricultural and Forest Meteorology*, *150*, 684–691.

Roderick, M. L., & Farquhar, G. D. (2004). Changes in Australian pan evaporation from 1970 to 2002. *International Journal of Climatology*, *25*, 1077–1090.

Santos, A. J. B., Quesada, C. A., Da Silva, G. T., Maia, J. F., Miranda, H. S., Miranda, A.C., et al. (2004). High rates of net ecosystem carbon assimilation by Brachiara pasture in the Brazilian Cerrado. *Global Change Biology*, *10*(5), 877–885.

Scott, R. L., Hamerlynck, E. P., Jenerette, G. D., Moran, M. S., & Barron-Gafford, G. (2010). Carbon dioxide exchange in a semi desert grassland through drought-induced vegetation change. *Journal of Geophysical Research—Biogeosciences*, *115*, G03026. http://dx.doi.org/10.1029/2010JG001348.

Scott, R. L., Jenerette, G. D., Potts, D. L., & Huxman, T. E. (2009). Effects of seasonal drought on net carbon dioxide exchange from a woody-plant-encroached semiarid grassland. *Journal of Geophysical Research—Biogeosciences*, *114*, G04004. http://dx.doi.org/10.1029/2008JG000900.

Segal, M., Jia, X., Ye, Z., & Pielke, R. A. (1990). On the effect of daytime surface evaporation on pollution dispersion. *Atmospheric Environment*, *24A*(7), 1801–1811.

Shuttleworth, W. J., Gurney, R. J., Hsu, A. Y., & Ormsby, J. P. (1989). FIFE: The variation in energy partition at surface flux sites. In A. Rango (Ed.), *Remote sensing and large scale processes*, Proceedings of the IAHS third international Assembly, Baltimore, MD, May. *IAHS Publication*, *186*, 67–74.

Slatyer, R. O., & Mcllroy, I. C. (1961). *Practical micrometeorology*. Melbourne, Australia: CSIRO (310 pp.).

Small, E. E., & Kurc, S. A. (2003). Tight coupling between soil moisture and the surface radiation budget in semiarid environments: Implications for land atmosphere interactions. *Water Resources Research*, *39*(10). http://dx.doi.org/10.1029/2002WR001297.

Small, E. E., & McConnell, J. R. (2008). Comparison of soil moisture and meteorological controls on pine and spruce transpiration. *Ecohydrology*, *1*, 205–214.

Strasser, U., & Mauser, W. (2001). Modelling the spatial and temporal variations of the water balance for the Weser catchment 1965–1994. *Journal of Hydrology*, *254*, 199–214.

Su, Z. (2002). The surface energy balance system (SEBS) for estimation of turbulent heat fluxes. *Hydrology and Earth Systems Sciences*, *61*(1), 85–99.

Sugita, M., Usui, J., Tamagawa, I., & Kaihotsu, I. (2001). Complementary relationship with convective boundary layer model to estimate regional evaporation. *Water Resources Research*, *37*(2), 353–365.

Sulkava, M., Luyssaert, S., Zaehle, S., & Papale, D. (2011). Assessing and improving the representativeness of monitoring networks: The European flux tower network example. *Journal of Geophysical Research*, *116*. http://dx.doi.org/10.1029/2010JG001562.

Tobin, D. C., Revercomb, H. E., Knuteson, R. O., Lesht, B.M., Strow, L. L., Hannon, S. E., et al. (2006). Atmospheric Radiation Measurement site atmospheric state best estimates for Atmospheric Infrared Sounder temperature and water vapor retrieval validation. *Journal of Geophysical Research*, *111*, D09S14. http://dx.doi.org/10.1029/2005JD006103.

Troufleau, D., Lhomme, J. P., Monteny, B., & Vidal, A. (1997). Sensible heat flux and radiometric surface temperature over sparse Sahelian vegetation. I. An experimental analysis of kB^{-1} parameter. *Journal of Hydrology*, *188–189*, 815–838.

Twine, T. E., Kustas, W. P., Norman, J. M., Cook, D. R., Houser, P. R., Meyers, T. P., et al. (2000). Correcting eddy-covariance flux underestimates over a grassland. *Agricultural and Forest Meteorology*, *103*, 279–300.

Veenendaal, E. M., Kolle, O., & Lloyd, J. (2004). Seasonal variation in energy fluxes and carbon dioxide exchange for a broad-leaved semi-arid savanna (Mopane woodland) in Southern Africa. *Global Change Biology*, *10*(3), 318–328.

Venturini, V., Islam, S., & Rodriguez, L. (2008). Estimation of evaporative fraction and evapotranspiration from MODIS products using a complementary based model. *Remote Sensing of Environment*, *112*(1), 132–141.

Wan, Z., Zhang, Y., Zhang, Q., & Li, Z. -L. (2004). Quality assessment and validation of the MODIS global land surface temperature. *International Journal of Remote Sensing*, *25*(1), 261–274.

Weaver, H. L. (1990). Temperature and humidity flux-variance relations determined by one dimensional eddy correlation. *Boundary Layer Meteorology*, *53*, 77–91.

Williams, C. A., Hanan, N., Scholes, R. J., & Kutsch, W. (2009). Complexity in water and carbon dioxide fluxes following rain pulses in an African savanna. *Oecologia*, *161*(3), 469–480.

Ye, Z., & Pielke, R. (1993). Atmospheric parameterization of evaporation from non-plant-covered surfaces. *Journal of Applied Meteorology*, *32*, 1248–1258.